

Local recurrent circuits modulate visual center and surround interactions in the mouse superior colliculus

Peng Cui^{1*}, Kuisong Song^{2*}, Dimitris Mariatos-Metaxas¹, Arturo G. Isla^{3,4}, Teresa Femenia², Iakovos Lazaridis⁵, Konstantinos Meletis¹, Arvind Kumar^{1,6} and Andreas A. Kardamakis^{1,2,#}

¹*Department of Neuroscience, Karolinska Institute, Stockholm, Sweden*

²*Instituto de Neurociencias CSIC-UMH, San Juan de Alicante, Spain*

³*Tecnológico de Monterrey, Escuela de Medicina y Ciencias de la Salud, México*

⁴*Department of Neurobiology, Care Sciences and Society, Karolinska Institute, Sweden*

⁵*McGovern Institute, Massachusetts Institute of Technology, Cambridge, USA*

⁶*Division of Computational Science and Technology. School of Electrical Engineering and Computer Science. KTH Royal Institute of Technology, Stockholm, Sweden*

* These authors contributed equally to the work

#Corresponding author

Send correspondence to:

Andreas Kardamakis
Instituto de Neurociencias CSIC-UMH
Avenida Santiago Ramón y Cajál s/n
San Juan de Alicante, 03015
Spain

Email:

akardamakis@umh.es
andreas.kardamakis@ki.se

Web:

<https://in.umh-CSIC.es/en/grupos/neural-circuits-in-vision-for-action/>
<https://ki.se/en/neuro/team-kardamakis>

Abstract

Extraretinal circuits can shape visual center-surround interactions that originate in the retina, yet the contributing circuit mechanisms to this initial modulation remain elusive. Using an optogenetic-based approach applied to the superficial layers of the superior colliculus (SCs), we demonstrate that the SCs is sufficient in generating surround suppression through selective patterned activation of visual center and surround zones in individual neurons. Like in the primary visual cortex, surround network activation causes decreases in center excitation rather than increases in synaptic inhibition. We reveal the identity of a SCs-based circuit with two interacting circuit motifs, recurrent excitation and

feedback inhibition, capable of modulating levels of center excitation when the visual surround is active, using whole-cell recordings, trans-synaptic mapping, and functional approaches with computational modeling. We propose that early subcortical and cortical visual circuits have evolved to perform surround modulation independently, thereby enhancing visuospatial versatility across multiple levels.

Introduction

Enabling neurons to compare central inputs with their immediate surround represents a fundamental and conserved computation (Churchland & Sejnowski, 1990; Grossberg, 1983). Termed 'surround modulation' and usually suppressive, it is found widespread across sensory modalities such as vision (Angelucci et al., 2017), hearing (Knudsen & Konishi, 1978), somatosensation (Sachdev et al., 2012), and olfaction (Olsen & Wilson, 2008). A typical example found across species is during size tuning of a visual neuron; the firing response initially increases when a stimulus is centered on its receptive field (Hubel & Wiesel, 1959; Schiller & Koerner, 1971), but then decreases as the stimulus expands beyond this area (Kardamakis et al., 2015; Kasai & Isa, 2016; McIlwain & Buser, 1968; Schiller & Stryker, 1972). This process relies on the interplay between excitatory cells releasing glutamate and inhibitory cells releasing GABA (γ -aminobutyric acid). As intuition would suggest, surround suppression can be mediated by increases of levels of GABAergic inhibition, however, different neural systems may assume different mechanisms (Carandini & Heeger, 2012). For example, similar to the findings in this study, surround suppression in the primary visual cortex is driven by decreases in levels of excitation rather than increases in synaptic inhibition (Sato et al., 2016). Understanding this mechanism but also the underlying local motifs used to implement surround modulation is necessary to understand how feedback from higher areas can manipulate visuospatial processes, such as for visual saliency (X. Zhang et al., 2012) and pop-out (Ahmadlou et al., 2017) or target selection in overt (McPeek & Keller, 2004) and covert attention (Wang et al., 2022).

Although surround modulation is observed across both visual thalamocortical in the lateral geniculate nucleus (Bonin et al., 2005), primary visual cortex (Jones et al., 2001) and extrastriate cortex (Born & Bradley, 2005), and in retinotectal systems in the optic tectum (Fernandes et al., 2021; Kardamakis et al., 2015, 2016) or superior colliculus (Kasai & Isa, 2016; Schiller & Koerner, 1971), its origin in the retina (Flores-Herr et al., 2001; Kim et al., 2022; Solomon et al., 2006; Y. Zhang et al., 2012) suggests that certain effects are likely fed forward to later stages of the visual hierarchy. Just as the primary visual cortex can participate in surround modulation within the thalamocortical system (Adesnik et al., 2012), we demonstrate that early visual circuits in the SCs can also participate independently within the retinotectal pathway. To reveal the circuit mechanism, we first customized an optogenetic-based electrophysiological approach in *ex vivo* that allows for center-surround interrogation and found that modulation is mediated by decreases in levels of excitation in absence of any increase in synaptic inhibition, resembling computations of divisive normalization (Carandini

& Heeger, 2012; Sato et al., 2016). We found the underlying functional circuit motifs between local excitatory (E) and inhibitory (I) neurons using cell-type-specific trans-synaptic mapping and key recurrent interactions using large-scale computational modelling. Finally, we identified functional shifts in the E/I balance in the surround when the center was active by using *in vivo* cfos induction with optogenetics, thus confirming a key model prediction. Taken together, our results suggest that phylogenetically older and newer early visual circuits based in SCs and V1 are both capable of performing surround suppression independently while using similar computational strategies in implementing center and surround interaction.

Results

Visual surround network activation modulates center excitability in the SCs

To establish the mechanism and circuit basis of visual surround modulation in mouse superior colliculus (SCs), we sought out to replicate center and surround network interactions in an *ex vivo* experimental setting by substituting physiological visual stimulus patterns with optogenetically-induced retinotopic impulse patterns (Fig. 1). By leveraging the aligned topographic correspondence of the retinotectal pathway (McLaughlin & O’Leary, 2005), we generated an input-dependent visual field. We made it light-excitable in the SCs by injecting an adeno-associated virus intravitreally that expressed ChR2 in RGCs of both wild-type C57BL/6NCrl ($n = 22$, $N = 14$) and vGAT-Cre ($n = 7$, $N = 5$) mice (see top panel, Fig. 1a). To ensure sufficient expression of ChR2 across the SCs, pan-retinal transfection was an essential prerequisite for trial inclusion (Bottom left, Fig. 1a); partial expressions were not taken into consideration. We mapped the receptive fields of single SCs neurons ($n = 29$, $N = 19$), referred herein to as center zones (C), by detecting subregions that triggered excitatory postsynaptic currents (EPSCs) in response to site-specific light patterns, which would activate the retinotopically arranged ChR2-expressing RGC axonal terminals in coronal SCs sections (Bottom right, Fig. 1a).

Given the *a priori* unknown perimeter of each center zone, which is contingent on the dendritic field of each neuron, the surround zone (S) can exhibit significant spatial variability and extend over a wide area (Fig. 1b-c). To accurately cover each neuron’s center zone and ensure a significant surround area, it was essential to create a sufficiently large field of view (FOV) that could accommodate their distinct morphologies. To do this, we decided to use one-photon widefield optics via a low magnification objective (16 \times) while using an in-house built dual-focus visual inspection system to selectively magnify or demagnify the optical path (Fig. 1b); a combination difficult to achieve with other approaches such as two-photon. Demagnification (by 0.5 \times) captured a large field of view (FOV) of $> 1\text{mm}^2$ that incorporated most of the SCs (magenta box in lower right of Fig. 1a), thus allowing for patterned micro-optostimulation of the entire visual layer. The other path diverted the light for magnification (by 2 \times), thereby achieving single cell resolution, which was sufficient to visually target our neurons of interest in whole-cell configuration (Fig. 1b). This approach allowed us

to delineate spatial patterns defining center and surround regions of single neurons, which were subsequently used to selectively activate separately or in sequences during recordings.

Figure 1c illustrates the center zone of a vGAT+ horizontal cell, which was determined by measuring evoked EPSCs after optostimulation (5 impulses at 10 Hz) of a 10×10 grid covering the FOV. The areas that evoked EPSC amplitudes exceeding 20% of the peak value (see Supplementary Fig. S1), which usually encompassed the soma and proximal dendritic processes, collectively formed an image pattern that was classified and used for center stimulation (Bottom left, Fig. 1c; see also Supplementary Fig. S1 and S4). Selective activation of this center zone always triggered short-latency compound EPSCs (mean amplitude: 120.8 ± 15.5 pA) characterized by prominent multimodal peaks (see arrowheads in the magenta trace in Fig. 1d), suggesting the presence of local recurrent connectivity amongst excitatory neurons in addition to the monosynaptic RGC input (Fig. 2-3).

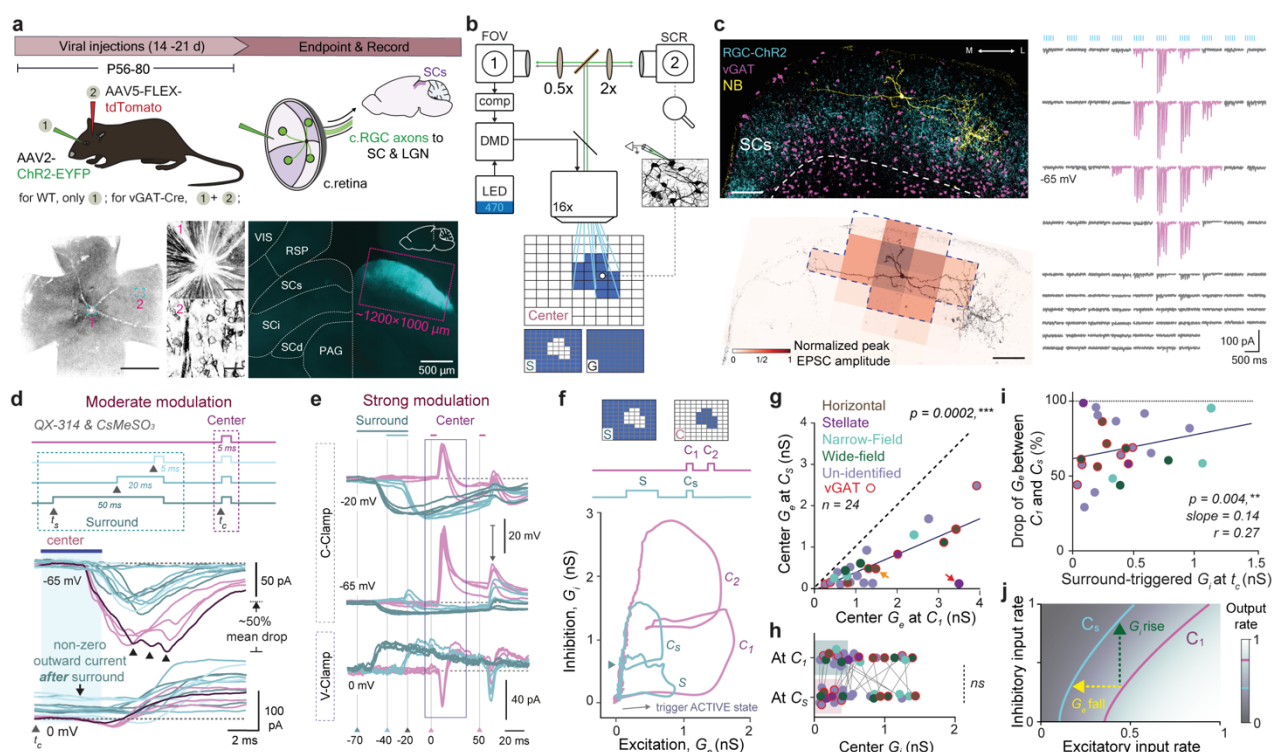


Fig. 1: Visual surround network activation modulates center excitability in SCs cell-types.

a, Top: Procedure showing expression of ChR2 in RGCs using an intravitreal viral injection of the vector rAAV2-hsyn-hChR2(H134R)-EYFP P (in WT mice, $N=22$) and unilateral labeling of contralateral SCs inhibitory neurons with the vector rAAV5-FLEX-tdTomato (in the case vGAT-Cre mice were used, $N=7$). Bottom left: Inverted fluorescent image of whole retinal mount confirming homogeneous RGCs transfection with ChR2-EYFP. Scale bar: 1200 μ m. Insets show enlarged aspects of the optic disc (1) and individual RGCs (2). Scale bar: 25 μ m. Bottom right: Coronal midbrain section with ChR2-expressing RGC axonal terminals seen occupying the SCs layer. **b**, A dual magnification setup enabling the simultaneous visualization of a large field of view (FOV) encompassing the SCs layer, and single cell resolution (SCR) for identifying excitation zones using whole-cell recordings and patterned optostimulation via a digital mirror device (DMD). See experimental procedures and Fig. S1-S4. **c**, Top left: a representative example of this approach applied to an inhibitory horizontal SCs neuron stained intracellularly with Neurobiotin (NB). Scale bar: 100 μ m. The neuron responds with excitatory

postsynaptic currents (EPSCs, shown in magenta) to a 20 Hz 5-light-pulse train delivered pseudo-randomly as a $120 \times 100 \mu\text{m}$ grid optostimulation (shown on the right). Bottom left: reconstructed neuron is shown with the denoted excitation zone (dotted line), which is referred to as center (C), whereas the non-responsive areas as surround (S) zone. **d**, Synaptic modulation between the center and surround zone of the neuron shown in **c**. Top: Temporal patterns underlying surround and center interaction. Bottom: Individual traces of synaptic inward and outward currents evoked in response to the center when recording at reversal equilibria for GABA_A-chloride mediated inhibition and glutamatergic excitation (-65 and 0 mV, respectively). Arrowheads show EPSC recurrence. Scale bar: 100 μm . Full traces in Fig. S2. **e**, Voltage traces revealing the strong modulation that the surround exerts on center activity in a stellate SCs interneuron. Voltage responses during surround followed by center (green traces) at two membrane holding potentials (-20 mV and -65 mV, top and middle, respectively) or during center alone (magenta). Bottom: Current traces when holding at 0 mV using the same condition. **f**, Plot of the inhibitory conductance as a function of the excitatory conductance in the neuron shown in **c** and **d**. Arrow shows direction of process when neuron is activated. **g-h**, Comparison of synaptic excitatory (**g**) and inhibitory (**h**) conductances between conditions: center only (C_1) and center after surround (C_s). Color coding corresponds to morphologically or genetically identified SCs neuron cell-types. Orange and red arrows depict data points from neurons shown in **d** and **e**, respectively. **i**, Modulation of center excitation plotted as a function of inhibitory conductance that is present at the time of center optostimulation (t_c). **j**, Schematic showing how the same level of response suppression can be achieved by either decrease in excitatory conductance or by increase in the inhibitory conductance. The gray colormap indicates a 2-D input-output transfer function of a neuron as a function of normalized input excitation and inhibition. The two curved lines indicate iso-firing rate contours. Statistical comparisons were performed as paired *t*-tests followed by Wilcoxon rank-signed tests. Abbreviations: *c.*, contralateral; *WT*, wild-type; *RGC*, retinal ganglion cell; *VIS*, primary visual cortex; *RSP*, retrosplenial cortex; *SCs*, superior colliculus superficial layer; *SCI*, superior colliculus intermediate layer; *SCd*, superior colliculus deep layer; *PAG*, periaqueductal gray matter.

To induce center-surround interactions, we first optostimulated the surround using three different durations and onsets (see dotted box in Fig. 1d). The surround-stimulation phases were terminated 20 ms before center-stimulation onset to ensure adequate time for the build-up of surround-induced activity while allowing for signal synchronization with the center-induced activity (cyan traces in Fig. 1d; see also Fig. S3d). Obviously, within these experimental settings, simultaneous center and surround activation, akin to whole-field (global) stimulation (Fig. 2h), would mask any discernible effect the surround would have on the center due to latency disparities. Comparing the magenta and cyan traces in Fig. 1d reveals a distinct and consistent decline in center responsiveness after surround activity, seen by a significant reduction in center-evoked EPSC amplitudes (~50% decrease in this recorded cell) along with a concurrent decrease in the number of multimodal peaks. In lines with previous studies (Kardamakis et al., 2015; Phongphanphanee et al., 2014), these evoked EPSCs were rapidly followed by a feedforward inhibitory component (mean amplitude \pm s.e.m.: $24.3 \pm 5.0 \text{ pA}$) observed at the equilibrium potential for glutamate-mediated excitation (0 mV, bottom of Fig. 1d), and here we observe that it occurred regardless of the presence of a preceding surround.

The degree of surround modulation varied across different SCs neurons. Based on the intensity of the reduction in center EPSC amplitude, the suppression was classified as mild, moderate or strong (Fig. 1d-e; strong: > 60%, $n = 9/24$; moderate: 20-60%, $n = 10/24$; mild: < 20%, $n = 5/24$). Figure 1e shows the voltage and current traces of a stellate SCs interneuron that was subject to a strong surround influence (see Supplementary Fig. S2 and S4). When its surround was activated, visual

input arriving to the neuron's center zone (top and middle traces) was completely suppressed by an outward current pulling its membrane potential toward the reversal for chloride-mediated GABA_A (γ -aminobutyric acid type A) inhibition (~69 mV; see bottom traces in Fig. 1e). Notably, the precise relative timing between surround (t_s) and center stimulation onsets (i.e., -70, -40, or -25 ms) or surround stimulation duration (5, 20, or 50 ms) had little impact on the amplitude variance of surround-triggered inhibitory postsynaptic currents (see arrow, Fig. 1d) or on the relative impact of center modulation. This mainly stems from latency differences in signaling between center and surround with surround E and I conductances peaking at average latencies of 20 and 28 ms, whereas center conductances peaked at 9 and 15 ms, respectively (Supplementary Fig. 3d).

Surround network activation typically generated a variable combination of excitation and inhibition in terms of amplitude and timing. However, during the onset of center stimulation (t_c), only the inhibitory components persisted while any remaining excitation was extinguished due to the relatively faster transmission of synaptic excitation (see Supplementary Fig. 2). This can be seen by the non-null values of surround-triggered outward currents when holding at 0 mV at t_c (see arrow, Fig. 1d and 1i). As expected, removal of surround input via pharmacological blockade of GABA_A receptors using bath-applied gabazine (GBZ) transformed any input into seizure-like activity while saturating subsequent center response profiles (bottom traces in Fig. S2a).

To test how surround signaling can account for the observed modulation of center excitability, we calculated the theoretical contributions of excitatory (G_e) and inhibitory (G_i) synaptic conductances (Wehr & Zador, 2003) during center only (magenta) and center-surround interaction (cyan) in Figure 1f. Here, the relationship between inhibition and excitation of the recorded neuron plotted in Figure 1d is shown during these two conditions (see also Fig. S3). Notably, consecutive center stimulations (C_1-C_2) reveal that inhibition can increase to nearly double the levels while simultaneously maintaining twice the levels of excitation compared to the significantly decreased levels evoked by surround-center stimulation ($S-C_s$). This result suggests that center-surround interactions conspire to reduce the persistence of both types of inputs. This was true for the majority of SCs interneuron cell types, with over half of them being classifiable based on either morphology (i.e., horizontal, wide-field, narrow-field, or stellate; for details, see Gale and Murphy, 2014) or genotype (e.g., vGAT+; see Fig. S4 for quantification). We found that peak excitation (G_e : mean amplitudes of C_1 : 1.7 ± 0.3 nS and C_s : 0.6 ± 0.1 nS with a mean percentage decrease of $62.3 \pm 4.7\%$) and peak total conductance (G_t : mean amplitudes of C_1 : 2.1 ± 0.3 nS and C_s : 1.2 ± 0.2 nS with an average percentage decrease of $40.6 \pm 5.3\%$) of the center response was significantly reduced following visual-driven surround network activity in all these recordings (Fig. 1g and Fig. S3), while no significant accompanying increase was observed on average to the center peak inhibition at peak G_t (Fig. 1h; mean amplitudes of C_1 : 0.53 ± 0.08 nS and C_s : 0.55 ± 0.09 nS).

There are two explanations for this weakening of the center excitatory conductance: (i) inhibitory conductances persisting at t_c , which might act linearly or non-linearly, and/or (ii) by a lesser number of active inputs arising from local glutamatergic interneurons contributing to the center response. While a weak, yet statistically significant, correlation was measured between the inhibitory conductance present at t_c (mean amplitude \pm s.e.m.: 0.46 ± 0.08 nS) and the percentage drop in center peak G_e (Fig. 1i), it could only partially explain the observed decrease. Both center and surround zones reciprocally affect each other through synergistic recurrent interactions among local populations of excitatory and inhibitory neurons, aiming to reduce the overall levels of excitation in the system (Fig. 1j).

SCs space defined by local recurrent excitatory and inhibitory circuit motifs

At the network level, reduction of center activity can be achieved by: 1) direct activation of long-range inhibitory neurons in the surround, 2) indirect activation of inhibitory neurons in the center via excitatory neurons in the surround, or 3) a combination of both connections. To reveal the underlying circuit motifs, we performed retrograde trans-synaptic labeling to identify their monosynaptic and presynaptic excitatory and inhibitory input neurons. Considering their comparable proportions (i.e., 40% vGluT2 and 60% vGAT; see (Liu et al., 2023)) and their intermingling within the SCs, we opted for genetically restricted approaches to accurately target and classify these neurons based on their cell type.

To trace local afferent input to excitatory and inhibitory neurons restricted within the boundaries of the SCs layer, an AAV-DIO-TVA-V5-RG was microinjected (50 nL) into the SCs of adult (older than 58 days) vGluT2- and vGAT-Cre mice (Fig. 2a and Fig.S5). This Cre-dependent AAV helper vector was designed to express the TVA receptor together with the engineered rabies glycoprotein (RG; see (Ährlund-Richter et al., 2019; Lazaridis et al., 2019) exclusively in either excitatory or inhibitory neurons, depending on the mouse line used, such as vGluT2- or vGAT-Cre, respectively. The injection of the helper virus was delivered into the SCs layer to ensure that neurons expressing the RG would be located within the SCs, as indicated by the green box in the coronal midbrain section of Figure 2b. Any cases where expression extended beyond the boundaries of the SCs were excluded from the analysis. Three weeks later, the enhanced green fluorescent protein (EGFP)-expressing rabies (Rb; see (Wickersham et al., 2007) viral vector was injected, targeting the same location in the SCs as the helper virus injection (Fig. 2a-b).

Neurons that were transfected with the Cre-dependent helper virus, as detected by V5 immunohistochemistry, which would also express Rb-EGFP were referred to as 'starter' neurons (Top, Fig. 2c). Therefore, in experiments involving vGluT2-Cre animals ($N = 3$), vGluT2+ excitatory cells served as starter neurons, while in experiments with vGAT-Cre animals ($N = 3$), vGAT+ inhibitory cells were the starter neurons. On the other hand, cells labeled solely with Rb-EGFP,

without the presence of the V5 tag, were classified as input neurons, providing monosynaptic input to the starter neurons (Fig. 2c). Rather than performing a whole-brain input analysis in the SCs (see (Reinhard et al., 2019), we focused on cracking the local connectivity between vGluT2+ and vGAT+ neurons in the SCs. We quantified the total number of presynaptic inputs (Fig. 2c; see also Fig. 2g) and examined the spatial distribution (Fig. 2e-f) onto each other, as well as long-range inputs arising from both retinas.

We found that vGluT2+ and vGAT+ starter neurons received a similar number of inputs from ipsilateral SCs interneurons (mean \pm s.e.m.: 9.5 ± 2 and 10.2 ± 2.8 cells, respectively) but also long-range inputs from both contralateral (2.9 ± 0.3 and 2.8 ± 0.7 cells, respectively) and ipsilateral RGCs (0.07 ± 0.01 and 0.03 ± 0.02 cells, respectively). As expected, the retinotopic pattern is observed (right of Fig. 2b), with contralateral RGC input mainly originating in central regions and ipsilateral RGC input restricted to peripheral regions of the retina, reflecting our systematic viral targeting of the middle region along the mediolateral (ML) and anteroposterior (AP) axes of the SCs (Fig. 2a and 4a). To determine whether the Rb-EGFP+ input cell types were excitatory or inhibitory, we performed RNAscope *in situ* hybridization (ISH) targeting the vesicular GABA transporter (vGAT) or the vesicular glutamate transporter 2 (vGluT2; Fig. 2b and 2d). Figure S5 shows that co-staining Rb-EGFP+ cells with vGluT2 and vGAT probes did not display colocalization, while nearly all input cells (269 out of 272 in $N = 2$ animals) were labeled using these two probes only. Therefore, we safely assumed that neurons that were negative for vGAT, were positive for vGluT2 and vice versa.

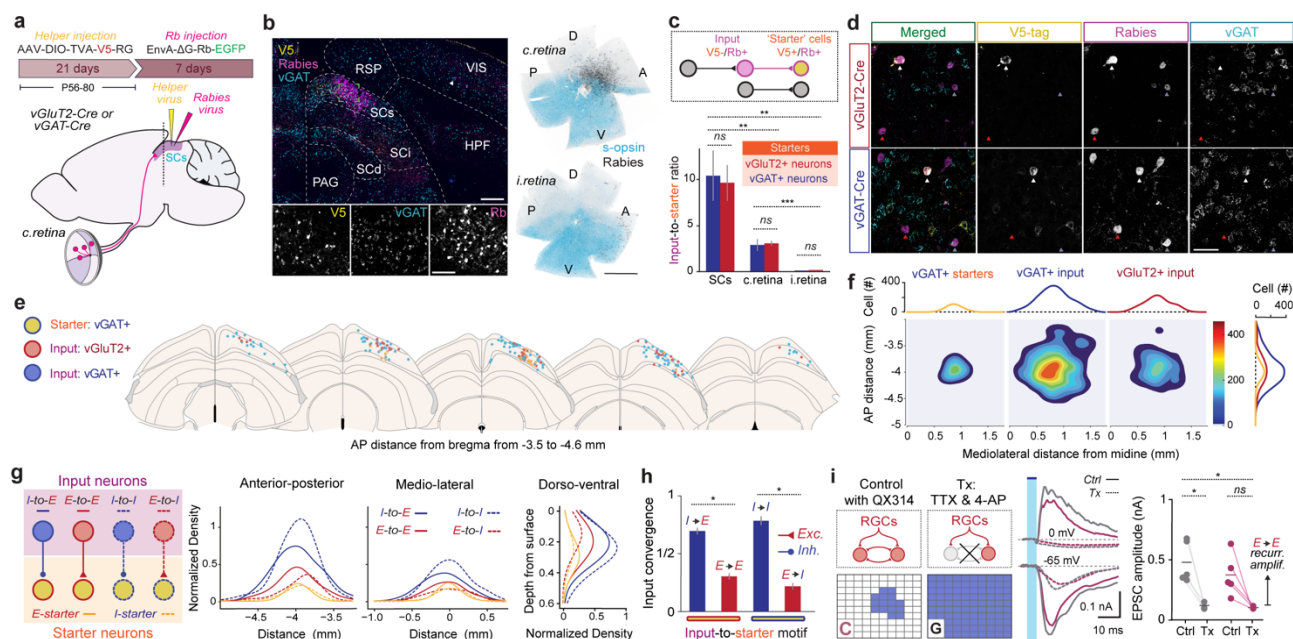


Fig. 2: Connectivity between local excitatory and inhibitory motifs in SCs space

a, The helper virus AAV-DIO-TVA-V5-RG expresses the rabies glycoprotein (RG), and a fusion of the TVA receptor with the V5 tag. The RG-deleted rabies virus Rb, pseudotyped with EnvA, expresses EGFP. The AAV helper virus was first injected into vGluT2-Cre ($N=3$) and vGAT-Cre ($N=3$) mice and 3 weeks later the Rb-EGFP was delivered in the same location in the SCs. **b**, Left: coronal section of the midbrain of a vGAT-Cre animal with emphasis on initial injection site where expression of the V5 tag (in

yellow) should be restricted to and not beyond the SCs layer. Subsequently, EGFP-expressing neurons are a result of Rb-transfection (magenta). Scale bar: 300 μm . Insets below show colocalization of the enlarged area (green box). Scale bar: 100 μm . Right: Contralateral and ipsilateral retinas showing retinotopy of presynaptic Rb-EGFP RGCs (black). Counterstaining with s-opsin (in light blue) reveals retinal orientation. Dorsal, D; anterior, A; ventral, V; posterior, P. Scale bars: 1000 μm . **c**, Top: starter neurons are identified based on the co-expression of the V5 tag and Rb-EGFP. Input neurons only express Rb-EGFP and provide monosynaptic and presynaptic input to the starter neurons. Bottom: Input convergence shows the ratio of input-to-starter neurons arising from: i) within the SCs, ii) contralateral (c.), and iii) ipsilateral (i.) retina. **d**, RNAscope ISH for vGAT (and vGluT2, *not shown*) revealed the identity of Rb-EGFP input neurons while confirming starter neuron cell-types. White arrows indicate starter neurons, whereas red and blue show excitatory (*E*) and inhibitory (*I*) input neurons, respectively. Scale bars: 50 μm . **e**, Schematic depicting the dorsoventral and mediolateral location of starter and input neurons in five separate anterior-posterior (AP) coronal sections of the SCs layer in a vGAT-Cre animal. **f**, Contour plot showing the spatial distribution of *E* and *I* input neurons to *I* starter neurons (for case shown in **e**) in the AP and medio-lateral ML dimensions across the SCs. **g**, (Left to right) Schematic of possible motifs between input and starter neurons. The next three panels show the quantitative relationship between the density of input neurons and starter neurons for both *E* and *I* cell types across the three anatomical dimensions (AP, ML and DV). Solid lines depict data obtained from excitatory starters averaged from $N=3$ vGluT2-Cre animals, whereas dashed lines show data obtained from inhibitory starters averaged from $N=3$ vGAT-Cre animals. See Supplementary Fig. S5e for the distributions obtained from individual animals. **h**, Quantitative cell-type-specific input-to-starter ratios (i.e., input convergence) reveal feedforward (i.e., *E*-*I* and *I*-*E*) and recurrent connectivity patterns (i.e., *E*-*E* and *I*-*I*). Comparison of means performed using Student's *t*-test. **i**, Excitatory and inhibitory current recordings (at -65 and 0 mV) from SCs neurons ($n=5$) were performed in response to center (C) and global (G) optostimulation conditions of RGC ChR2-expressing presynaptic axons. Bath application of 1 μM TTX and 100 μM 4-AP isolate monosynaptic RGC-triggered excitation while abolishing the functional impact of recurrent excitation and recruited feedforward inhibition. Mean evoked EPSC amplitudes \pm s.e.m.: from left to right, for Ctrl: 0.40 ± 0.08 nA; for Tx: 0.02 ± 0.01 nA; for Ctrl: 0.29 ± 0.08 nA; for Tx: 0.010 ± 0.004 nA. RM one-way ANOVA, $p = 0.0072$; Tukey's multiple comparisons test, $p(\text{global-Ctrl v.s. global-Tx}) = 0.0382$, $p(\text{global-Ctrl v.s. center-Tx}) = 0.0308$, $p(\text{center-Ctrl v.s. center-Tx}) = 0.0821$. Washout not shown for clarity. Abbreviations: HPF, hippocampal formation; Ctrl, control condition; and Tx, treated condition.

The relative spatial distributions of vGluT2+ and vGAT+ starter and input neurons were determined by counting the neurons expressing V5 and/or RV-EGFP and we mapped their location onto the Allen Reference Atlas (ARA) coordinate system across the SCs layer (Fig. 2e-f and Supplementary Fig. S5e; see Methods for details). In Figure 2e, a representative example of a vGAT-Cre animal is shown, illustrating a small number of concentrated inhibitory starter neurons (V5+ and Rb-EGFP+; depicted as yellow dots) together with a broader distribution of input neurons (Rb-EGFP+), which were further classified based on their neurotransmitter type as excitatory (red dots) or inhibitory (blue dots). For all the animals, every 6th section was imaged (14 μm in thickness, 10-16 sections per animal) and subsequently co-registered to the corresponding ARA coordinate. We determined the mediolateral, anteroposterior, and dorsoventral distribution using this approach for each starter and input neuron, as well as their respective cell type classification (Supplementary Fig. 5e).

The Gaussian kernel-based density plots in Figure 2f reveal the horizontal distribution patterns along the ML and AP dimensions (see Methods) of the representative example shown in Figure 2e. Inhibitory starter neurons (left panel in Fig. 2f) were observed to occupy a confined retinotopic area within the SCs, influenced monosynaptically by a broader excitatory area (right panel in Fig. 2f), as well as an even broader inhibitory area (middle panel), thereby, receiving visual input from RGCs

located across larger retinal regions. At peak density, the inhibitory starters were found to receive synaptic input from more than double as many inhibitory input neurons establishing a motif of recurrent inhibition (Fig. 2f).

Using this approach applied across animals ($N = 6$), we found that all potential motifs between input and starter neurons exist (Fig. 2g and Supplementary Fig. 5e) were connected with similar input-to-starter ratios (Fig. 2h). In Figure 2g, color-coded solid lines represent average spatial distributions using excitatory neurons as starters, while color-coded dashed lines correspond to those from inhibitory starters (see Fig. S5e for individual traces). As expected, input neurons always display higher normalized density distribution compared to their starter counterparts. Notably, while $I-E$ and $I-I$ input-to-starter connections span a broader range on the ML, AP and DV axes, a stable E/I ratio is maintained throughout the SCs, with no identifiable asymmetries arising from a specific connection. In comparison to excitatory neurons, inhibitory inputs exhibited stronger connections with other inhibitory starter neurons ($78.8 \pm 4.6\%$, $n = 3$) and excitatory starter neurons ($69.2 \pm 2.3\%$, $n = 3$), with the remaining proportion accounted for by excitatory input neurons. Notably, about one third of excitatory input neurons establish monosynaptic contact with excitatory starter neurons (second column in Fig. 2g), thereby, establishing a local recurrent excitatory network that can be also triggered by monosynaptic long-range RGC input (Fig. 2b).

Figure 2i demonstrates the efficacy of this $E-E$ connection by recording SCs neurons ($n = 5$) in response to optostimulation of RGC terminals within their identified center zones in the presence of $1 \mu\text{M}$ TTX and $100 \mu\text{M}$ 4-AP (washout *not shown* for clarity). Evoked EPSC amplitudes were drastically reduced by about $\sim 90\%$, with a small component persisting resulting from monosynaptic RGC input (Fig. 2i, mean amplitudes \pm s.e.m.: for Ctrl: $405.5 \pm 81.1 \text{ pA}$; for Tx: $22.3 \pm 11.0 \text{ pA}$). This observation suggests the existence of additional center-dependent excitatory input (Fig. 2d, 2g-h and S5e), which may serve to amplify incoming visual signals. Furthermore, the lack of observed outward currents (traces held at 0 mV) during this treated condition (Tx) indicates the removal of recruited di- or oligo-synaptic inhibition, thereby exposing the indirect functional impact of local $I-E$ and $I-I$ inputs (Fig. 2i). As expected, the similar response profiles observed between center-specific and whole-field (global) optostimulation indicate that most of the $E-E$ input is generated within the neuron's center zone.

Local recurrent excitation and feedback inhibition drives visual surround suppression

To isolate the contribution of different connections ($E-E$, $E-I$, $I-I$, and $I-E$) to the center-surround interactions in Figure 1d-j, we constructed a large-scale model consisting of 12,800 spiking neurons to simulate the SCs layer. The model was constrained by the measured input convergence ratios (Fig. 2g-h, Supplementary Fig. 5e) summarized in the cartoon in Figure 3a. To quantify these network interactions, we used a spiking neuron model with conductance-based synapses, which

were connected to each other based on physical distance between according to a Gaussian connectivity kernel (see Table 3 and Supplementary Fig. S4e). Because we were interested in the contribution of different connections, we kept the connection probability and distance-dependent connectivity kernel fixed and systematically varied the connections strengths (see Table 3-7). For all synaptic strengths the network remained in an inhibition-dominated activity regime in which inhibitory neurons displayed a higher background activity than excitatory neurons (Gehr et al., 2023).

To mimic center zone activation, we triggered activity in 314 excitatory and 314 inhibitory model neurons in four conditions (Fig. 3b-d) and measured the evoked excitatory synaptic conductance in a randomly chosen neuron from the center region (Fig. 3e). First, the center neurons alone were stimulated (see no.1 in Fig. 3b, top row in Fig. 3c and first column in Fig. 3d). As with our experimental recordings (see Fig. 1d), model center response patterns typically demonstrated multiple peaks, often characterized by a dual peak profile (green trace in Fig. 3e). The first peak is provided monosynaptically by glutamatergic RGC input and followed by a second one that indicates that center stimulation engaged activity in neighboring unstimulated excitatory neurons. As expected, the second peak depended mainly on the strength of recurrent excitatory connection (*E-E*), yet it also covaried with the strength of the (*I-E*) connectivity (Fig. 4f).

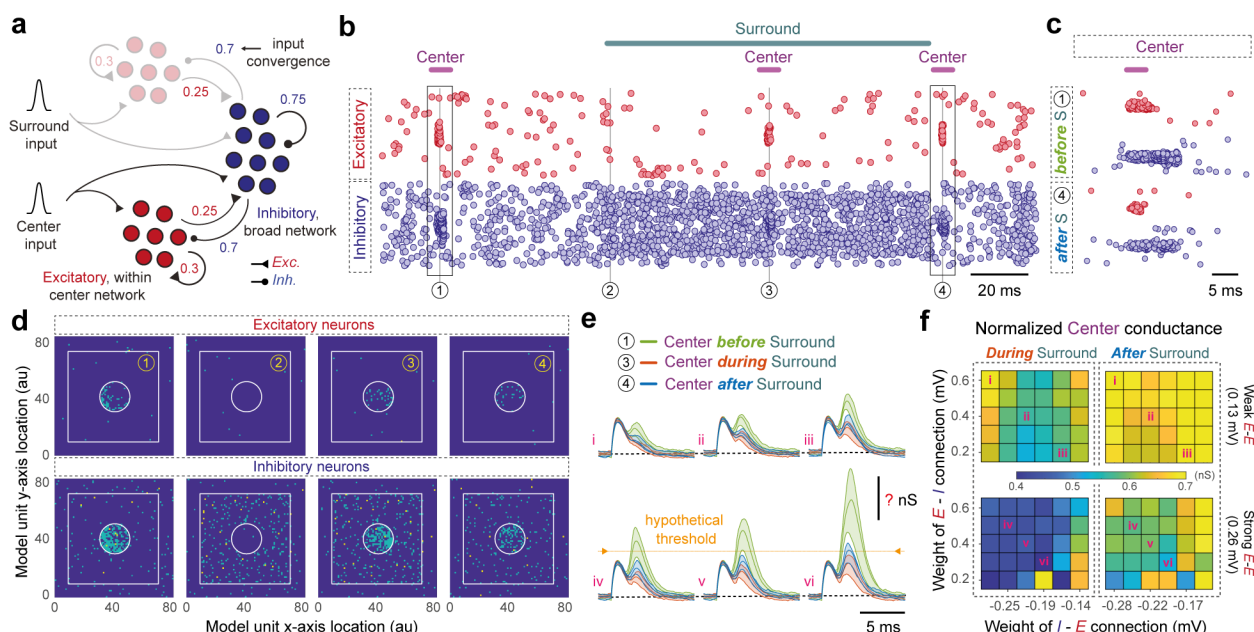


Fig. 3: Model predicts recurrent networks a key feature in visual surround modulation

a, Schematic of the network model using E/I connectivity patterns (Fig. 2g). 6400 excitatory and 6400 inhibitory neurons were placed on a square lattice which was folded as a torus to avoid boundary effects (see **c**). **b**, Raster of spiking activity with four stimulus conditions that are marked with vertical numbered lines (1: center only before surround, 2: surround only, 3: center during surround, and 4: center after surround) that simulate experimental conditions shown in Fig. 1. **c**, Expanded network response of conditions 1 (top) and 4 (bottom) shown in **b**. **d**, Spatial arrangement of center and surround network response profiles during the 4 different stimulus impulse conditions. The square schematically shows the region in which neurons were placed on a square grid. Excitatory (top) and inhibitory neurons (bottom) within the white circle received inputs corresponding to the center stimulation. All the neurons in white square but outside the inner circle received inputs corresponding to the surround network. Each subplot

shows activity measured within a 5 ms bin. **e**, Time courses of excitatory conductance of a center neuron. Each trace is an average of 20 trials and shading indicated 25%-75% quartiles. The first peak is generated with low-variance monosynaptic activation of direct retinal input whereas the second peak is a network effect generated by balanced recurrent excitation and recurrent inhibition. The connectivity parameters for these six examples are marked in panel **f** with Latin numerals. **f**, Reduction in the excitatory conductance due to surround inputs. Each colormap shows normalized change in excitatory conductance (see Methods) in a center neuron (shown in panel **e**) as a function of recurrent excitation (top: weak connection; bottom: strong connection) and mutual connectivity between excitation and inhibition (x-axis: inhibition of excitatory neurons; y-axis: excitation of inhibitory neurons).

When center stimulation was immediately followed by a surround input (see #4 in Fig. 3b, bottom row in Fig. 3c and fourth column in Fig. 3d), the peak of the secondary response was determined by the mutual coupling between excitatory and inhibitory neurons (blue traces in Fig. 3e). In line with our results presented in Fig. 1, the initial surround-induced inhibitory conductance persisted after the removal of surround inputs, effectively attenuating the secondary response to below threshold (yellow line in Fig. 3e) since fewer neurons (both *E* and *I*) could respond beyond threshold to the center input (bottom row in Fig. 3c). This was further supported by the observation that secondary response attenuation was more pronounced when center input coincided with the presence of surround input (red traces in Fig. 3e). Even though center and global responses are comparable in amplitude (Fig. 2i), confirmation of this prediction was not possible experimentally as center responses would prevail during the simultaneous optogenetic activation of center and surround (see #3 in Fig. 3b and third column in Fig. 3d).

To quantify the contribution of individual circuit motifs, we normalized the center response during and after surround input (left and right column in Fig. 3f) by the peak when only center input was delivered (Fig. 3f). As expected, any increase in the *I-E* connection increased its attenuation, whereas *E-I* connectivity did not have a strong effect on the attenuation of the secondary peak. Notably, increase in the strength of recurrent excitation also increased the attenuation of the secondary excitatory conductance peak (compare top and bottom rows in Fig. 3f). The effect of surround-triggered inhibition on center excitation was larger when center input arrived in the presence of an active surround (left column in Fig. 3e). Overall these results demonstrate the reduction in excitatory conductance during surround suppression requires both recurrent *E-E* and *I-E* connections.

Center activation lowers E/I balance of active SCs neurons in the surround

Results obtained from the circuit mapping (Fig. 2c and 2g-h) corroborated with the simulated network (Fig. 3e-f) indicate that the balance between excitation and inhibition (E/I) should shift to lower values in the surround region when the center is stimulated. To test this prediction, we intravitreally injected wild-type C57BL/6NCrl mice with an AVV2-ChR2-EYFP ($N = 5$) or AAV2-mCherry ($N = 3$, for control) to express ChR2 (or a control protein) in RGC axonal terminals (top, Fig. 4a). The successful activation of SCs neurons following *in vivo* optostimulation of RGC terminals via an

implanted fiber optic unilaterally was confirmed through *cFos* labeling, a surrogate marker of neural activity (Fig. 4a-b). The animals were maintained in a dark chamber to eliminate the potential influence of natural visually driven activity.

Figure 4b shows the distribution of active SCs cells in coronal sections (top is control, bottom is ChR2). After control optostimulation, the presence of a sparse population of spontaneously active neurons located could be seen reflecting baseline activity at approximate equidistant locations along the mediolateral axis with a higher concentration near the midline (top image in Fig. 4b). Optostimulation of ChR2-expressing RGC axonal terminals (bottom image in Fig. 4b; see Methods) revealed a significant increase in *cFos* expression under the implant (top, Fig. 4c), with higher overall levels observed across both hemispheres (bottom, Fig. 4c). Furthermore, an asymmetrical distribution of *cFos* expression across the hemispheres was observed, whereas in absence of the opsin (control) the distribution maintained symmetry (bottom, Fig. 4b).

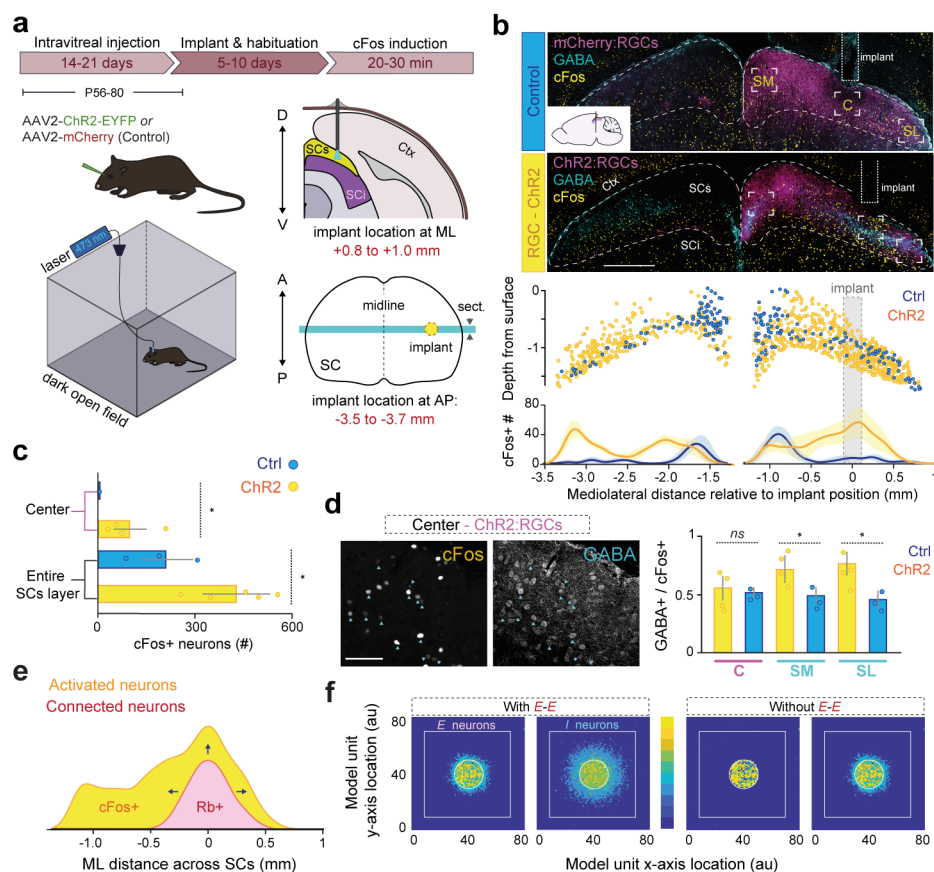


Fig. 4: Functional identification of active SCs neurons reveals that center activation lowers E/I balance in the surround

a, Pipeline and schematics that we used to measure *in vivo* *cFos* expression resulting from local optostimulation of RGC axonal terminals in the SCs. Top left: As in Fig. 1a, expression of ChR2 in RGCs was achieved using an intravitreal viral injection of the vector rAAV2-hsyn-hChR2(H134R)-EYFP (in WT mice, $N=5$) or rAAV2-hsyn-mCherry for control (in WT mice, $N=3$). Bottom left: schematic illustrating assay performed in a dark box. Right panels: cartoon of the optic fiber placement site shown in a coronal (top) and a horizontal (bottom) midbrain sections. **b**, Top panels: Coronal midbrain sections of the SCs centered around the implant for *cFos* induction following local optostimulation. Yellow, *cFos*

immunostaining; magenta, control (top) or ChR2 (bottom); cyan, GABA immunostaining. Scale bar represents 500 μm . Abbrev: C, center; SM (surround medial); SL (surround lateral). Bottom panels: The location (top) and distribution (bottom) of c-Fos positive neurons across the hemispheres of the SCs. Blue circles are control; Yellow circles are ChR2-induced. The central zone (C) is defined by the implant tip, which defines the origin of the x-axis. Shading is standard error. **c**, Comparison of the total cell count of cFos+ cells induced in SCs neurons between control (in blue, $N=3$) and during activation of ChR2-expressing RGC axonal terminals (in yellow, $N=5$), both across the entire SCs layer and center zone. **d**, Top: Grayscale image taken from the center region showing cFos (left) and GABA immunostaining (right). Blue arrows show colocalization. Bottom: Ratio of GABA+ to cFos+ across the three zones (C, SM and SL) compared between the two conditions (ChR2-induced, $N=4$; and control, $N=3$). Statistical testing was done using Student's *t*-test (*, $p < 0.01$; ***, $p < 0.0001$; ns, no significance). Bars show standard error of the mean. **e**, Comparison of the distribution between activated and connected neurons. Plot of activated neurons (in yellow) was obtained from the bottom right panel in **b**, whereas the plot of connected neurons (in red) was obtained using cell-type-specific transsynaptic retrograde mapping shown in Fig. 2 and Supplementary Fig. 5. **f**, Qualitative comparison of the effect of variable recurrent E-E connection strengths (strong, top; weak, bottom) on the distribution of active neurons in response to center stimulation using the same model parameters used in Fig. 3. The square schematically shows the region in which neurons were placed on a square grid (as in Fig. 3d). Center: inner circle. Surround: Within the inner white square excluding the area occupied by the white circle. Probability of spiking (estimated from 20 trials) of a neuron when center alone was stimulated. The color bar ranges from 0 to 1 and shows the probability of spiking when the center is stimulated. Abbreviations: C, center; SM, surround medial; SL, surround lateral.

Shifts in E/I balance was determined by quantifying the proportion of inhibitory neurons among the total activated cells. To do this, we defined the center region as the area located directly under the implant (C), along with two distal surround zones located more than 500 μm from the center: a medial surround zone (SM) and a lateral surround zone (SL). Figure 4d (top) shows a subset of cFos positive neurons in the center zone that were immunoreactive for the neurotransmitter GABA revealing their inhibitory origin (see also Supplementary Fig. S7). Notably, optostimulation drives a balance of excitation and inhibition in the center with a population of putative glutamatergic neurons (i.e., negative for GABA) that matches the population size of active inhibitory neurons (C: 0.49 ± 0.07 , $N = 4$; mean \pm s.e.m.). The fraction of colocalized neurons, however, shows a significant increase in the ratio of active GABAergic neurons in both surround zones compared to the center (SM: 0.70 ± 0.13 , SL: 0.73 ± 0.14 , $N = 4$; mean \pm s.e.m.). This finding suggests that there will be fewer recurrent excitatory neurons present to amplify visual signals in the surround when the center is active, and conversely.

This E/I drop in the surround gives rise to another issue as to signal propagation from the center to the surround. Figure 4e shows the spatial distribution between activated neurons (data from Fig. 4b) and connected neurons (data from Fig. 2g and Supplementary Fig. S5e). Given the unlikely event of activated fibers of passage targeting areas other than the center (Hong et al., 2011), which may contribute to this discrepancy, two more plausible reasons can be identified: 1) activation of retinotopically aligned recurrent networks and/or 2) activation of upstream circuits connected to the SCs (Fig. 4e).

In order to explore the potential of this connectivity footprint, we replicated the experimental setting by increasing the intensity of the model's center stimulation while utilizing the same parameters as depicted in Fig. 3 (refer to Table 5 for details). When recurrent excitatory connections were strong (top row in Fig. 4f), center stimulation also drove neuronal activity in the surround that was not directly stimulated as indicated by non-zero firing probability in neurons outside the white circle depicting the model 'center' (Fig. 4f). Recruited responses in inhibitory neurons spread out more than in excitatory neurons indicating the spatial discrepancy between the *E-E* and *E-I* connections, which is independent of center size. This qualitative description obtained by the model simulation can explain shifts in surround E/I without the exclusive reliance on long-range horizontal connections.

Discussion

Targeted optogenetic activation of center and surround zones in individual neurons allowed us to test the presence and circuit implementation of surround modulation, using the SCs as a conserved model of early visual processing. Our experiments show that a selective decrease in center excitation occurs when the visual surround is active (Fig. 1); a potential computation contributing to midbrain target selection where a current central input becomes the next saccade's surround input. Given our experimental settings, this result proves that evoked changes in synaptic excitatory conductance of varying magnitude (usually moderate or strong) are due to local interactions placed within the midbrain SCs itself. This finding suggests that main extraretinal circuits (i.e., SCs and V1) belonging to divergent pathways can perform surround suppression separately prompting the question of whether a stimulus can be selectively suppressed in one pathway while simultaneously preferred in the other.

As in cortical circuits (Niell & Scanziani, 2021), the SCs also contains excitatory and inhibitory neurons that are spatially intermingling and distributed over its layer; features that complicate the cracking of their function. By combining intracellular measurements (Fig. 1) and connectivity analysis (Fig. 2) with a computational model (Fig. 3), we revealed two main local circuit motifs: recurrent excitation (*E-E*) and feedback inhibition (*I-E*) that contribute to surround suppression in distinct ways. *E-E* connections amplify responses in a specific retinotopic 'center' whereas *I-E* performs a dual function. It overlaps with center-specific *E-E*, thereby modulating the responses of the same center neurons subject to *E-E*, while simultaneously, reaching slightly beyond this zone, curbing the responsiveness of neighboring surround neurons outside the center (Fig. 2–3). In natural conditions, however, every input should be accompanied by some surround input since one neuron's center will be another neuron's surround. We show that in such a case, these recurrent interactions conspire to reduce the persistence of input in the absence of top-down input. Further research is required to establish whether multiple classes of inhibitory interneurons are involved in specific computations in the SCs, drawing parallels to findings in V1 where the potential role of somatostatin-positive neurons in surround suppression was identified (Adesnik et al., 2012).

Visual center-surround interaction in the SCs provide cortical circuits the flexibility to modulate SCs circuitry either by amplifying or suppressing local activity across the visual map of collicular space (see white arrow in Fig. 2b, see also (Ahmadlou et al., 2017)). This could allow them to engage with SCs recurrent networks and modulate local center-surround dynamics in a top-down manner. For instance, by granting selective access for pyramidal neurons in V1 to interact with *E-E* connections, responses can be biased to specific incoming retinal inputs from certain areas of the visual field, or in contrast, they can be suppressed by activating *I-E* connections. Importantly, these phylogenetically conserved circuits in the SCs can also influence cortical activity via tecto-thalamic pathways (Brenner et al., 2023), thereby influencing visual attention (Wang & Krauzlis, 2018; Zénon & Krauzlis, 2012). This highlights the ability of SCs activity to modulate neural activity in both upstream and downstream targets, potentially influencing higher-order functions like visuospatial perception and behavioral selection.

The question of whether these networks process all visual streams uniformly, with each stream conveyed by distinct RGC subtypes (of which more than 30 are known, see (Baden et al., 2016), can be addressed using a similar approach presented in this study. For instance, can some inputs bypass this circuitry, evade surround suppression, and avoid engaging *I-E* subcircuits? Can they selectively drive surround facilitatory connections for contour integration across the visual layer (Kapadia et al., 1995)? This can be addressed by optostimulating specific RGC subtypes using opsins expressed in specialized Cre-lines (e.g., Kcng4-Cre for targeting alpha RGCs, see (Krieger et al., 2017)), instead of a panretinal approach. This rationale can be taken beyond sensory systems, interrogating the presence and nature of center-surround interactions in modular architectures within motor systems that would be technically challenging to address *in vivo*. The *ex vivo* approach demonstrated in this study can provide key insight into local circuit function and underscores the need for developing approaches that link such local processes to global network function.

Taken together, our results show that this selective decrease in center excitation when the visual surround is active is consistent with models that involve amplification in recurrent networks (Douglas et al., 1995), but inconsistent with models that are dominated by feedback inhibition (Harris & Mrsic-Flogel, 2013). In the latter, transient increase in inhibition would account for reduction in overall excitation and inhibition levels – an outcome that our measurements did not support. Computational models of trial-by-trial variability suggest that, while both increases in inhibition or decreases in recurrent excitation can similarly affect the average output response, the latter is more likely to minimize variability across trials (Guo & Kumar, 2023). We propose that tectal circuitry has evolved to mitigate this variability where surround inputs are continuously transformed into center inputs during visual exploration.

Acknowledgements

We thank Dr. Sten Grillner for his support throughout this study. We thank Dr. Mats Hellström for his assistance with intravitreal surgeries. A.A.K. acknowledges funding from the Swedish Research Council (Starting Grant in Medicine no. 2016-03134 and Project Grant in Medicine no. 2020-02927), CIDEVENT funding from the Valencian Community in Spain (no. 2021-028), Strategic research area neuroscience StratNeuro (Start-up program 2017), the Swedish Brain Foundation (Hjärnfonden no. FO2018-0254), the Hedlunds Foundation (no. M-2017-0691) the Olle Engvist Foundation (no. 196-0148) and the Stiftelsen Kronprinsessan Margeratas Arbetnämnd för synskadade (nos. 2019-027 and 2020-182).

Author Contributions

P.C. performed electrophysiological recordings, viral injections, optogenetic experiments and data analysis. K.S. performed neuroanatomical experiments, RNAscope *in situ* hybridization, viral injections, fiber implantations and data analysis. D.M.M. performed *in vivo* cFos induction experiments, visualization of neuroanatomy, and data analysis. A.G.I. performed electrophysiological recordings. I.L. and T.F. contributed to neuroanatomy and *in vivo* experiments. A.A.K. performed the conductance analysis. I.L., K.M., T.F., and A.A.K contributed to the conceptualization and experimental study design. K.M. contributed vectors and resources for visualization of neuroanatomical data. A.K. contributed to the computational study design and performed the numerical experiments. A.A.K. designed the figures, supervised and funded the study. A.A.K. wrote the manuscript with help from A.K. All authors reviewed and commented on the manuscript.

Material and Methods

Animals

Experimental procedures were approved by the 1) Stockholm municipal committee for animal experiments and the Karolinska Institute in Sweden (N9179-2017 and N6747-2019 to A.A.K.) and 2) the Committee on Animal Research at the Universidad Miguel Hernández and carried out in compliance with the Research Council of Spain (CSIC), the Generalitat Valenciana (GVA) and European regulations (2022/VSC/PEA/0236 to A.A.K.). Both male and female vGAT-Cre (Jackson: Slc32a1tm2(cre)Lowl), vGluT2-Cre (Jackson: Slc17a6tm2(cre)Lowl) and wild-type mice (C57BL/6N; Charles River) were used throughout the experiments. Mice were kept on a 12-h day/night cycle under stable temperature ($21 \pm 1^\circ\text{C}$) and air humidity (50–65%) with freely available food and water. The exact numbers of cells (n) and animals (N) used for each experiment are reported in the *Results* section and corresponding figure legend.

Viral injections

The complete list of viruses we used is provided in Supplementary Table 1. Injections were performed in 2–5 months old wild-type mice and transgenic mice under isoflurane anesthesia and injected with buprenorphine post-surgery. Viral titers of adeno-associated viruses (AAV) and modified rabies virus were between 1×10^{12} and 1×10^{13} viral genomes per milliliter (vg/mL). To express ChR2 in the axons of RGCs in the superficial layer of the right hemisphere SC, we injected 1000 nL into the vitreous bodies of the left retinas using the following viral vectors:

- 1.rAAV2/hsyn-hChR2(H134R)-EYFP-WPRE-PA (UNC Vector Core),
- 2.rAAV2/hsyn-hChR2(H134R)-mcherry-WPRE-PA (UNC Vector Core),
- 3.rAAV2-EF1 α -DIO-hChR2(H134R)-EYFP (UNC Vector Core), or
4. ssAAV-2/2-shortCAG-dlox-hChR2(H134R)_EYFP(rev)-dlox-WPRE-hGHP(A) (VVF, Zurich).

We used the vector rAAV2/hsyn-mcherry (UNC Vector Core) as in our control group for the intravitreal injections. To identify GABAergic neurons in the SCs, the vector rAAV5-CAG-FLEX-tdTomato (400 nL, UNC Vector Core) was injected into two collicular sites in order to maximize expression: 1) the rostral SCs (from bregma: anteroposterior (AP) -3.6 mm; right (R) -0.8 mm; dorsoventral (DV) -1.6 mm from the surface of the skull), and 2) the caudal SCs (AP -4.2 mm; R -1.8 mm; DV -1.5 mm) respectively on the same day.

For the rabies viral tracing, 50 nL of helper virus AAV5-EF1a-DIO-TVA-V5-t2A-RG was injected into the right SCs (AP -3.9 mm; R -0.8 mm; DV -1.05 to -1.15 mm from the surface of the brain) in vGAT-Cre or vGluT2-Cre mice, while taking great care to maintain viral spread to within the SCs layer. Three weeks later, 150 nL of the engineered rabies virus EnvA-coated G-deleted rabies virus with EGFP (EnvA- Δ G-Rb-EGFP) was injected into the same location.

For secondary injections, fiber optic implantations and electrophysiological recordings, two to three weeks were allowed to pass after the initial injection. Viral suspensions were delivered at 500 nL/min and 100 nL/min for intravitreal and brain injections, respectively. A puncture was made 2 mm posterior to the corneal limbus using a sterile 30-gauge (G) needle after pupil dilation was achieved with 0.5% Alcaine. After which 1000 nL vitreous was aspirated manually using a Hamilton microliter syringe. The glass capillary was then inserted through the same puncture by using a microliter syringe (1.5 mm volume) into the eye, and the tip was angled toward the vitreous humor and back of the eye, taking care to avoid any damage to the retina or lens. The capillary remained in the eye for 2 min in order to prevent reflux of the viral suspensions. Brain injections were performed by using a digital stereotaxic frame combined with a Quintessential Stereotaxic injector (Stoelting) via a glass capillary. The capillary firstly reached 0.2 mm deeper than the target location to give space

for the viral suspensions, then was slowly retracted to the target location to complete the injections. Afterwards, the capillary was retracted by 0.2 mm again and remained in position for 8 min. During the injections, all the mice were kept on a heating pad at 37 °C with a subcutaneous injection of buprenorphine while maintaining the eyes were moisturized with Viscotears gel.

Whole-cell electrophysiology with DMD-based dual camera optostimulation system

The animals were deeply anaesthetized by using a combination of pentobarbital injected intraperitoneally. To ensure rapid cooling of the midbrain, we perfused the animals transcardially with an ice-cold cutting solution, containing the following (in mM): NaCl 40, KCl 2.5, NaH₂PO₄ 1.25, NaHCO₃ 26, glucose 20, sucrose 37.5, HEPES 20, NMDG 46.5, Na L-ascorbic acid 5, CaCl₂ 0.5 and MgCl₂ 5 (pH 7.3 with HCl). The brain was rapidly dissected out after decapitation. Coronal midbrain slices (400 µm) were prepared by using a vibratome (VT1000S, Leica, Germany) in the cutting solution and incubated in the same solution at 35 °C for 12 min. The sections were subsequently maintained at room temperature in recording solution that contained the following (in mM): NaCl 124, KCl 2.5, NaH₂PO₄ 1.25, NaHCO₃ 26, glucose 20, CaCl₂ 2 and MgCl₂ 1 (pH 7.3). Cutting and recording solutions were continuously infused with carbogen (95% O₂ and 5% CO₂) throughout the procedure.

Whole-cell patch clamp recordings were either performed on random neurons in the SCs of wild-type mice or tdTomato-expressing neurons of vGAT-Cre mice at room temperature using pCLAMP 11 (Molecular Devices, USA). Midbrain slices were continuously perfused with oxygenated recording solution at a rate of 2 mL/min during recording and visualized under an upright CleverScope motorized microscope (Micro Control Instruments, UK) equipped with a Dodt gradient contrast system (DGC-2), an oil condenser (U-AAC, Olympus, Japan) and two Chameleon3 cameras (Teledyne FLIR, USA). Whole-cell recordings were obtained under visual control using a 16× (0.80 NA) water dipping objective (CFI75 LWD 16X W, Nikon, Japan) combined with 2× c-mount extender (EX2C, Computar, USA) and c-mount adapters (U-TV1X-2 and U-CMAD3, Olympus, Japan) with Axon MultiClamp 700B amplifier and Axon Digidata 1320A digitizer (Molecular Devices, USA). Signals were sampled at 20 kHz. Pipettes used for recording were pulled from borosilicate glass capillaries (article no. 1403542, Hilgenberg, Germany) by a P-97 Micropipette Puller (Sutter Instrument, USA). Patch pipettes (5–8 MΩ) were filled with a potassium gluconate based intracellular solution contained (in mM): K D-gluconate 125, EGTA 1, KCl 10, HEPES 10, ATP-Mg 4, GTP-Na 0.3, phosphocreatine 10, CaCl₂ 0.1 and QX314 3 (pH 7.2 with KOH; 290 mOsm). Due to the long recording times (usually one hour), the access resistance was evaluated every 10 min to ensure that initial values (only under ~30 MΩ were considered) did not increase throughout the recording session.

ChR2-expressing axons of retinal ganglion cells were optically stimulated with 470 nm light from a high-power collimated LED source (Mightex, Canada) connected to a digital mirror device (Polygon1000, Mightex, Canada) by a 3 mm-core liquid lightguide (Newport, USA). The stimulation patterns were triggered via Master-8 pulse stimulator (A.M.P.I, Israel) and designed via the software PolyScan2 (Mightex, Canada). TdTomato-expressing vGAT-positive neurons in the SCs were detected with 540 nm light from a high-power collimated LED source (Mightex, Canada) and an RFP filter set (Olympus, Japan). The 540 nm LED was connected to a 495 nm dichroic filter cube (Mightex, Canada) with the 470 nm LED during the transgenic animal experiments. Both LEDs were directed via a four channel BioLED light source control module (Mightex, Canada).

For membrane property measurements, a series of 1000 ms negative and positive injected current steps from -30 pA to +40 pA in 5 pA increments were delivered through the recording electrode under current-clamped conditions to each recorded neuron.

Optogenetic stimulation patterns were created and performed during the recordings by the digital mirror device (DMD), Polygon (Mightex, Canada). The 16 \times objective combined with the 2 \times front tube optics (Mightex, Canada) and 0.5 \times single photo port tube lens camera adapter (Olympus, Japan) enabled a large workable field-of-view ($\sim 1.2 \times 1$ mm working area). With this customized visual inspection system with this dual camera approach, whole-cell patch-clamp recordings were performed using the high magnification light pathway whereas optostimulations patterns could be performed using the low magnification pathway that enables the large field of view. All neurons were voltage-clamped at -65 and 0 mV to measure excitatory postsynaptic currents (EPSCs) and inhibitory postsynaptic currents (IPSCs) respectively. In most neurons, synaptic currents were also recorded at intermediate potentials (at -45 mV), when recordings were sufficiently stable.

For control experiments, whole-field stimulation patterns were delivered by 10 Hz trains of 8 stimuli (5 ms duration), followed by a single test stimulus at 5 s time interval, and each trace included four repetitive sweeps. For the center-surround experiments, SCs neurons were subjected to the following patterns: 'GridScan', 'Center-Center', 'Surround-Surround' and 'Surround-Center'. Center (C) and Surround (S) areas were determined by using the GridScan protocol, which was delivered 10 Hz trains of 5 light pulses of 5 ms duration in 100 non-adjacent grids arranged in a 10×10 spatial configuration across the FOV (0.1 \times 0.07 mm for each one). After the end of the GridScan, we promptly calculated the maximum EPSC and IPSC amplitudes for each grid after it was normalized and filtered using custom-written MATLAB (MathWorks). Excitatory postsynaptic current amplitudes arising from each grid location were thresholded on the basis of their evoked amplitude. Grid locations that yielded $\geq 10\%$ of the peak EPSC amplitude for the recorded neuron, were considered to be part of the center zone, whereas locations that did not pass this threshold were considered to be part of the surround zone. To trigger center-surround interactions, the surround was optostimulated by a single pulse that was then followed by a two or five-pulse train stimulation

delivered to the center. We experimented with a range of different surround stimulation durations (5, 20, 50 ms) and with a range of surround-center delays (0, 10, 20, 50 ms) to explore the parameter space. Data was obtained using intermediate values for most of the trials, thereby also avoiding technical issues or stimulation artifacts.

Drugs used in electrophysiology

Drugs were bath applied and an overall duration of at least 5 min was allowed before testing their effects, which was followed by a washout phase of at least 10 minutes. Unless otherwise indicated, drugs were perfused during patch-clamp recordings under the given conditions using a two-gauge peristaltic pump (Pretech Instruments, Sweden). The complete list of drugs used is provided in Supplementary Table 2.

Estimation of synaptic conductances

For the estimation of the synaptic conductances, we used a method described in Wehr and Zador (2004). To deconstruct inhibitory and excitatory synaptic conductance, recordings were performed during 'center-center', 'surround-surround', 'surround-center', and 'global' optostimulation. A Cesium-based QX314 solution was used in the recording pipette to improve intrinsic conductance isolation and block action potential discharge conditions (Fig. 1 and Supplementary Fig. 2-3). Evoked synaptic currents used in this analysis were obtained by averaging values from 5 to 10 sweeps for each recorded cell. Due to the long recording times (usually one hour), the access resistance was evaluated every 10 min to ensure that initial values (only under $\sim 30\text{ M}\Omega$ were considered) did not increase throughout the recording session. This procedure was repeated for two to three different potentials (-65 , -45 , and 0 mV) held with different levels of current injection. Customized Matlab scripts were written to estimate the total, excitatory and inhibitory synaptic conductances based on the equations used in Wehr and Zador (2004).

Neuronal reconstruction

To identify the dendritic fields from the recorded neurons, we used 0.3% Neurobiotin (Vector Laboratories, no.VESP-1120-50) in the intracellular solution during whole-cell recordings. We post fixed the midbrain slices and then used PBS to wash them. To visualize the neurons, we stained them with streptavidin Cy5 (1:400, Jackson ImmunoResearch, no. 016-170-084) and imaged them using confocal microscopy with a 20 \times objective (LSM-800, Zeiss, Germany). The images were processed with ImageJ software, and the neurons were reconstructed by using the plugin Simple Neurite tracer. The dendritic areas of each labeled neuron were calculated by tracing a convex polygon around the outermost tips of the dendritic field. The SC cell types were then classified on the basis of their geometry (Gale & Murphy, 2014).

Fiber optic implantation and cFos activation

Two weeks after the intravitreal injection, a 200 μm diameter fiber optic (Thorlabs, FG200UEA) was implanted into the right SCs (from bregma: AP -3.6 mm; R -1.0 mm; DV -1.0 mm from the brain surface). The mice recovered for at least one week before the cFos induction experiment. The mice were habituated to handling in an open field area (60 cm \times 60 cm \times 60 cm; WxDxH) and the connected optic fiber for at least 3 days before proceeding with the experiment. To minimize stress, bedding from the cage was placed in the box. Optogenetic stimulation was not initiated for 90 min after the mice were placed in the dark box to avoid any prior visual effects on the observed cFos expression. The RGC axonal terminals in the SCs were stimulated with a train of 1 s square pulses of 40 Hz frequency (10 ms ON and 15 ms OFF) every 10 sec for a total of 40 min. After the stimulation period, the mice were left undisturbed for 60-70 min to ensure sufficient cFos protein expression. A maximum of 90 min after the end of the stimulation period was allowed before the mice were euthanized with pentobarbital and perfused with ice-cold 4% paraformaldehyde (PFA) in 0.01 M (1 \times) phosphate-buffered saline (PBS) buffer. The brain and retinas were subsequently dissected, and post fixed in 4% PFA overnight at 4°C.

Immunofluorescent staining and *in situ* hybridization

Mice were anesthetized by pentobarbital and perfused with 1 \times PBS and 4% PFA. The brains (and eyes, to confirm pan-retina transfection) were harvested and fixed in PFA at 4 °C overnight, then washed with PBS for 3 times. The brain was placed in 15% sucrose solution for 24 h, then transferred into 30% sucrose solution for 24–72 h. The brains were subsequently embedded in optimal cutting temperature compound (OCT), frozen with dry ice and kept at -20 °C for short-term storage. The cryostat sectioning was performed on a Epredia NX70 cryostat. The brains, between the thalamus and brainstem, were sectioned in 14 μm thickness, about 80% (12 to 15) sections in the SCs were collected on glass slides, and every 6th section was sampled for the following staining (the interval is about 0.105 mm). The other parts of the brain were sectioned in 40 μm thickness and stored in 1 \times PBS with 0.01% sodium azide.

The fluorescence *in situ* hybridization was performed with RNAscope Multiplex Fluorescent Reagent Kit v2 (ACD, Cat. No. 323100). The probes for vGluT2 (Mm-Slc17a6-C2, ACD, Cat. No. 319171-C2) and vGAT (Mm-Slc32a1, ACD, Cat. No. 319191) were used to identify the cell types. The manufacturer's protocol was followed. Co-staining of vGAT and vGluT2 *in situ* hybridizations was also performed for control experiment, and the results were shown in Supplementary Fig. 5.

Immediately following the *in situ* hybridization, the brain sections were incubated in chicken anti-V5 primary antibody (Abcam, ab9113) in 1:750 at room temperature overnight, then washed with 1 \times TBST (0.3% TritonX-100), and incubated in donkey anti-chicken Cy3 secondary antibody (Jackson ImmunoResearch, no. 703-165-155) in 1:1000. All the antibodies were diluted with 1 \times TBST (0.3%

TritonX-100, 3% BSA, 0.01% sodium azide). After PBS washing and DAPI staining, the sections were mounted with an antifade mounting medium (VWR, BSBT AR1109). For the cFos staining, rat or rabbit anti-cFos primary antibodies (Synaptic Systems, no. 226-017 or no. 226-003, 1:500) and GABA primary antibody (Sigma-Aldrich, A2052, 1:2000) were used in 1× PBST (0.3% TritonX-100, 5% donkey serum, 0.01% sodium azide) at room temperature overnight, then the sections were stained with Cy3 donkey anti-rabbit (Jackson ImmunoResearch, no. 711-165-152) or AF647 donkey anti-rat (Jackson ImmunoResearch, no. 712-605-153). The same following steps are previously described.

The retinas were first removed from the eye in the perfused animals and then flattened with the help of four incisions, and finally washed in 1x PBS for 3 times. For the retina immunostaining, the retina was first treated with pre-heated (about 70 °C) 1× antigen retrieval citrate buffer (Sigma, C9999), then followed the same protocol as with the brain section described above. Rabbit anti-S-opsin primary antibody (Sigma, AB5407) and donkey anti-rabbit Cy3 secondary antibody were both used in 1:1000 to visualize the short-wave photoreceptors, which reveals retinal orientation.

Network model

Here, we used the integrate and fire model to simulate the dynamics of neurons. The subthreshold membrane potential (V_m) of each neurons was described by the following differential equation:

$$C_m dV_m/dt = g_L (V_m - E_L) + I^{bkg}_{syn} + I^{net}_{syn} + I^{stim}_{syn}$$

Where C_m is the membrane capacitance, g_L is the leak conductance, I^{net}_{syn} is the total synaptic input from neurons within the network, I^{bkg}_{syn} is the background input from other networks, I^{stim}_{syn} is input corresponding to center or surround inputs (see Supplementary Table 3). When the membrane potential reached V_{th} , spike was elicited and the V_m was reset to E_L for t_{ref} millisecond. In the network all neurons were identical. Neuron parameters are provided in Supplementary Table 4.

Synaptic inputs were modelled as conductance transients with following dynamics:

$$g_{syn} = J_{syn} t / \tau_{syn} \exp(-(t - (t_{spk} + d_{syn})) / \tau_{syn}) \text{ when } t - t_{spk} > 0 \text{ else } g_{syn} = 0.$$

Where t_{spk} is the spike time, d_{syn} is the synaptic delay, J_{syn} {syn: ee, ei, ie, ii, ex, ix} is the amplitude of the postsynaptic potential (PSP), and τ_{syn} is the synaptic time constant. In our model all synapses of a particular type (external, excitatory, or inhibitory) have the same parameters (see Supplementary Table 5). In our model we fixed the amplitude (J_{syn}) of the external excitatory (J_{ex}), inhibitory (J_{ix}) synapses and J_{ii} (inh. → inh.). The value of J_{ee} (exc. → exc.), J_{ei} (exc. → inh.), and J_{ie} (inh. → exc.) were systematically varied. Synapse parameters are provided in Supplementary Table 5.

We considered a network with 6400 excitatory and 6400 inhibitory neurons. Neurons were placed on an 80 × 80 grid. Because we have the same population size for the two neuron types, both types

of neurons were placed on the same size grid. Neurons were connected based on their spatial distance. To avoid boundary effects, the 80×80 grid was folded as a torus. The connection probability decreased as a function of distance according to a Gaussian function. The standard deviation of the Gaussian was set to 16 and 20 for excitatory and inhibitory synapses, respectively. This was based on our experimental data which showed that inhibitory neurons have a slightly bigger extent of their spatial connectivity than that of excitatory synapses (Fig. 2f). 16 and 20 grid points constitute 2% and 2.5% of our network space. The area of the Gaussian function (*i.e.* the total number of connections sent out by a neuron) was decided based on the input convergence we measured in our experiments (Fig. 2g-h). Network connectivity parameters are provided in Supplementary Table 6.

Each neuron received Poisson type excitatory and inhibitory spiking inputs to mimic inputs from outside the network and to obtain a low firing rate (< 1 Hz) background activity. See Supplementary Table 7 for parameters.

To model a short flash like input to the center region, we selected 314 excitatory and 314 inhibitory neurons, located in a circle (radius = 10 grid points) at the center of our network model. These neurons received a single synchronous spike from 10 presynaptic neurons (from the retina). Each spike elicited 1.1 mV depolarization. Each neuron received such a synchronous spike event at the stimulus onset (T_{center}). Each individual neuron received the synchronous spike event at a time $T_{center} + r$, where r is a random number drawn from a uniform distribution ($U[0,1]$). Center stimulus was presented to the neurons in three conditions: center only, center stimulus just at the end of the surround stimulus (see below) and center while the surround stimulus was still on. See Supplementary Table 3 for more details.

To mimic the surround stimulus, we selected 3286 exc. neurons and 3286 inh. neurons from a square region in the network with a side of 60 grid points. The center neurons (see above) were located at the center of this square. For the surround stimulus we excluded the center neurons. The surround stimulus was injected in the selected neurons in the form of uncorrelated Poisson type spike trains. See Supplementary Table 3 for more details.

The network model was simulated using the simulator NEST (Fardet et al., 2020).

Statistical analysis and data plotting

For each mouse, 10–16 sections were stained and visualized. Confocal images (20 \times) were used for the manual scoring of co-expression of vGAT/vGluT2, V5 and RV-GFP. Whole-brain images (10 \times) were acquired with a fluorescent microscope (Leica DM6000B) and a digital camera (Hamamatsu Orca-FLASH 4.0 C11440). They were manually registered to a bregma AP coordinate (from bregma -3.2 to -4.9), and subsequently aligned to the Allen Reference Atlas with the WholeBrain R package (Ährlund-Richter et al., 2019; Fürth et al., 2018). Every detected Rb-EGFP positive neuron was registered, and the coordinates were used for the following analysis. As the

main source of monosynaptic input and local input, only the RV-GFP positive cells in the SCs were included in the calculation. For the comparison between mice, the number of input neurons were normalized to the total number of detected Rb-EGFP positive neurons in SCs. All the density estimations were done using a Gaussian kernel and were then plotted in R.

To minimize the effects of M-L differences of the injection sites between animals, the centroid of the starter neurons was first computed using k-means clustering analysis, which then allowed us to plot the relative M-L coordinate for each neuron. As for the depth estimation, the coordinates of the SC surface were first obtained with the WholeBrain R package, then the depth of each neuron was calculated after subtracting the difference. In both, M-L and depth density plots, only 3 central brain sections with the highest starter density were included according to the AP density plot.

After confocal imaging the cFos fluorescence was quantified by a 3d object counter plug-in of Fiji. Colocalized cFos+ and GABA+ cells were manually counted in three areas in SCs (C, SM and SL; see Fig. 4). The statistical analysis and visualization were done in Python (code available upon request).

We used three model stimulation protocols: center only (center), center stimulus just at the end of the surround stimulus (center after surround) and center while the surround stimulus was still on (center with surround). Each paradigm was repeated 20 times. For each stimulus presentation, we recorded excitatory conductance from a single neuron. We estimated the across trial mean and variance of the conductance input to the recorded neuron. Finally, the results were rendered as the mean and variance of the excitatory conductance at specific time points after the onset of the stimulus in all three stimulus paradigms. In addition, we recorded spiking activity from all the neurons and estimated the firing rate of neurons. The network model was simulated using the simulator NEST. All differential equations were integrated using Runga-Kutta method with a time step of 0.1 ms.

Electrophysiology data analyses were performed using Clampfit 11 (Molecular Devices, USA), GraphPad Prism (GraphPad Software 7.00, USA), ImageJ (1.53c, NIH, USA), RStudio (R 3.6.1) or MATLAB (R2018b, MathWorks, USA). Data were all presented as mean values \pm s.e.m. Before performing paired *t*-test or one-way ANOVA analysis, the normality and the homogeneity of variance were first evaluated using Kolmogorov–Smirnov's test and Brown–Forsythe's test. If the *p* value of Kolmogorov–Smirnov's test was less than 0.05, Wilcoxon's signed-rank test would be used instead of paired *t*-test. If *p* value of Brown–Forsythe's test was less than 0.05, Friedman test and Kruskal–Wallis test would be used instead of a repeated-measures one-way ANOVA (RM one-way ANOVA) and ordinary one-way ANOVA, respectively. *p* values were corrected for deviation using the Geisser–Greenhouse correction. Once the *p* value of a one-way ANOVA analysis was less than 0.05, Tukey's multiple comparisons test would be performed. *F* and *df* (*df*1, *df*2) are degrees of freedom for one-way ANOVA and paired *t*-test, respectively. *p* values less than 0.05 were

considered significant with asterisks in figures denoting as follows: * $p < 0.05$, ** $p < 0.01$, *** $P < 0.001$, **** $p < 0.0001$, ns, no significance.

Supplementary Table 1. Viruses used in this study

Name	Type	Titer	Source
rAAV2/hsyn-hChR2(H134R)-EYFP-WPRE-PA	AAV2	5.6 × 10 ¹² vg/mL	UNC Vector Core
rAAV2/hsyn-hChR2(H134R)-mcherry-WPRE-PA	AAV2	5.1 × 10 ¹² vg/mL	UNC Vector Core
rAAV2-EF1α-DIO-hChR2(H134R)-EYFP	AAV2	4.4 × 10 ¹² vg/mL	UNC Vector Core
ssAAV-2/2-shortCAG-dlox-hChR2(H134R)_EYFP(rev)-dlox-WPRE-hGHp(A)	AAV2	1.4 × 10 ¹² vg/mL	ZNZ Viral Vector Facility
rAAV2/hsyn-mcherry	AAV2	5.3 × 10 ¹² vg/mL	UNC Vector Core
rAAV5-CAG-FLEX-tdTomato	AAV5	7.8 × 10 ¹² vg/mL	UNC Vector Core
AAV5-EF1a-DIO-TVA-V5-t2A-RG	AAV5	1.2 × 10 ¹² vg/mL	DMC laboratory
EnvA-ΔG-Rb-EGFP	Modified Rabies	1 × 10 ¹⁰ vg/mL	DMC laboratory

Supplementary Table 2. Drugs used in electrophysiology experiments

Compound	Drug name	Concentration	Source
Gabazine (SR 95531)	6-Imino-3-(4-methoxyphenyl)-1(6H)-pyridazinebutanoic acid hydrobromide	10 μM	Tocris Bioscience, USA
TTX	(4 <i>R</i> ,4 <i>aR</i> ,5 <i>R</i> ,7 <i>S</i> ,9 <i>S</i> ,10 <i>S</i> ,10 <i>aR</i> ,11 <i>S</i> ,12 <i>S</i>)-Octahydro-12-(hydroxymethyl)-2-imino-5,9:7,10a-dimethano-10 <i>aH</i> -[1,3]dioxocino[6,5- <i>d</i>]pyrimidine-4,7,10,11,12-pentol	1 μM	Tocris Bioscience, USA

4-AP	4-Aminopyridine	100 µM	Sigma-Aldrich
QX314	<i>N</i> -(2,6-Dimethylphenylcarbamoylmethyl)triethylammonium bromide	3 mM	Tocris Bioscience, USA

Supplementary Table 3. Stimulus input

Type of input	Stimulated neurons	Spike input	Stimulus PSP	Repeats
Center Input	All neurons (exc. and inh.) in a circle with radius 10 grid points. 314 exc. neurons and 314 inh. neurons.	Each neuron received 10 synchronous spikes corresponding to the presentation of a flash like center stimulus. Arrival time of each synchronous spike event was taken from a uniform distribution U[0,1] ms.	1.03 mV at -54 mV to exc. neurons 0.86 mV at -54 mV to exc. neurons	20
Surround input	All neurons (exc. and inh.) within a square of size 60 grid point centered at the center of the network. Neurons part of the center stimulus were excluded. 3286 exc. neurons and 3286 inh. neurons.	Poisson type spiking input with a spike rate of 100 Hz. Surround stimulus was presented for 200 ms.	2.58 mV at -54 mV	20
Surround input	All neurons (exc. and inh.) within a square of size 60 grid point centered at the center of the network. Neurons part of the center stimulus were excluded.	Poisson type spiking input with a spike rate of 50:10:130 Hz. Surround stimulus was presented for 200 ms.	2.58 mV at -54 mV	20

	3286 neurons 3286 neurons.	exc. and inh.			
--	-------------------------------	---------------------	--	--	--

Supplementary Table 4. Neuron parameters

Parameter	Value	Description
C_m	200 pF	Membrane capacitance
g_L	20 nS	Leak conductance
V_{th}	-54 mV	Spike threshold
E_L	-70 mV	Reversal potential for leak conductance
t_{ref}	2 ms	Refractory time

Supplementary Table 5. Synapse parameters

Parameter	Value	Description	Notes
J_{ex}	0.63 mV	EPSP amplitude for connection from external excitatory inputs	EPSP amplitude was measured at a holding potential of -54 mV
J_{ix}	-0.3 mV	IPSP amplitude for connection from external inhibitory inputs	IPSP amplitude was measured at a holding potential of -54 mV
J_{ee}	{0.13, 0.26} mV	EPSP amplitude for exc. → exc. connection	EPSP amplitude was measured at a holding potential of -54 mV
J_{ei}	{0.11, 0.21, 0.32, 0.42, 0.53, 0.63} mV	EPSP amplitude for exc. → inh. connection	EPSP amplitude was measured at a holding potential of -54 mV
J_{ie}	{-0.14, -0.17, -0.19, -0.22, -0.28, -0.3} mV	IPSP amplitude for inh. → exc. connection	IPSP amplitude was measured at a holding potential of -54 mV
J_{ii}	0.055 mV	IPSP amplitude for inh. → inh. connection	IPSP amplitude was measured at a holding potential of -54 mV

τ_{ae}	1.0 ms	Time constant of excitatory synapses	This was the same for both exc. → exc., exc. → inh. synapses and external excitatory input synapses
τ_{ai}	3.0 ms	Time constant of inhibitory synapses	This was the same for both inh. → exc., inh. → inh. synapses and external inhibitory input synapses
d_{ee}	0.2 ms	Synaptic delay for exc. → exc. synapses	
d_{ei}	0.1 ms	Synaptic delay for exc. → inh. synapses	
d_{ie}	0.1 ms	Synaptic delay for inh. → exc. synapses	
d_{ii}	0.1 ms	Synaptic delay for inh. → inh. synapses	

Supplementary Table 6. Network connectivity

Parameter	Value	Description	Notes
N_e	6400	Excitatory neurons	
N_i	6400	Inhibitory neurons	
Excitatory grid size	80×80	Neurons were placed on a regular grid	
Inhibitory grid size	80×80	Neurons were placed on a regular grid	
C_{ee}	0.135	Connection probability between exc. to exc. neurons. This number refers to the integral of the connectivity kernel	Based on our experimental data (See Fig. 2g)
C_{ei}	0.112	Connection probability between exc. to inh neurons. This number refers to the integral of the connectivity kernel	Based on our experimental data (See Fig. 2g)
C_{ie}	0.315	Connection probability between inh to exc. neurons. This number refers to the integral of the connectivity kernel	Based on our experimental data (See Fig. 2g)
C_{ii}	0.3375	Connection probability between inh. to inh. neurons. This number refers to the integral of the connectivity kernel	Based on our experimental data (See Fig. 2g)
S_e	16 grid points	Standard deviation of Gaussian used to estimate distance dependent	

	2% of the network size	connectivity from exc. to exc. and exc. to inh. neurons.	
S_i	20 grid points 2.5% of the network size	Standard deviation of Gaussian used to estimate distance dependent connectivity from inh. to exc. and inh. to inh. neurons.	

Supplementary Table 7. External Input

Parameter	Value	Description
nu_exc	1000 Hz	Poisson type spike trains were injected in all neurons
nu_inh	600 Hz	Poisson type spike trains were injected in all neurons

REFERENCES

- Adesnik, H., Bruns, W., Taniguchi, H., Huang, Z. J., & Scanziani, M. (2012). A neural circuit for spatial summation in visual cortex. *Nature*, 490(7419), Article 7419.
<https://doi.org/10.1038/nature11526>
- Ahmadolou, M., Tafreshiha, A., & Heimel, J. A. (2017). Visual Cortex Limits Pop-Out in the Superior Colliculus of Awake Mice. *Cerebral Cortex*, 27(12), 5772–5783.
<https://doi.org/10.1093/cercor/bhx254>
- Ährlund-Richter, S., Xuan, Y., van Lunteren, J. A., Kim, H., Ortiz, C., Pollak Dorocic, I., Meletis, K., & Carlén, M. (2019). A whole-brain atlas of monosynaptic input targeting four different cell types in the medial prefrontal cortex of the mouse. *Nature Neuroscience*, 22(4), Article 4. <https://doi.org/10.1038/s41593-019-0354-y>
- Angelucci, A., Bijanzadeh, M., Nurminen, L., Federer, F., Merlin, S., & Bressloff, P. C. (2017). Circuits and Mechanisms for Surround Modulation in Visual Cortex. *Annual Review of Neuroscience*, 40(1), 425–451. <https://doi.org/10.1146/annurev-neuro-072116-031418>

- Baden, T., Berens, P., Franke, K., Román Rosón, M., Bethge, M., & Euler, T. (2016). The functional diversity of retinal ganglion cells in the mouse. *Nature*, 529(7586), Article 7586. <https://doi.org/10.1038/nature16468>
- Bonin, V., Mante, V., & Carandini, M. (2005). The Suppressive Field of Neurons in Lateral Geniculate Nucleus. *The Journal of Neuroscience*, 25(47), 10844–10856. <https://doi.org/10.1523/JNEUROSCI.3562-05.2005>
- Born, R. T., & Bradley, D. C. (2005). Structure and Function of Visual Area Mt. *Annual Review of Neuroscience*, 28(1), 157–189. <https://doi.org/10.1146/annurev.neuro.26.041002.131052>
- Brenner, J. M., Beltramo, R., Gerfen, C. R., Ruediger, S., & Scanziani, M. (2023). A genetically defined tecto-thalamic pathway drives a system of superior-colliculus-dependent visual cortices. *Neuron*, 111(14), 2247-2257.e7. <https://doi.org/10.1016/j.neuron.2023.04.022>
- Carandini, M., & Heeger, D. J. (2012). Normalization as a canonical neural computation. *Nature Reviews Neuroscience*, 13(1), Article 1. <https://doi.org/10.1038/nrn3136>
- Churchland, P. S., & Sejnowski, T. J. (1990). Neural Representation and Neural Computation. *Philosophical Perspectives*, 4, 343–382. <https://doi.org/10.2307/2214198>
- Douglas, R. J., Koch, C., Mahowald, M., Martin, K. A., & Suarez, H. H. (1995). Recurrent excitation in neocortical circuits. *Science (New York, N.Y.)*, 269(5226), 981–985. <https://doi.org/10.1126/science.7638624>
- Fardet, T., Vennemo, S. B., Mitchell, J., Mørk, H., Gruber, S., Hahne, J., Spreizer, S., Deepu, R., Trensch, G., Weidel, P., Jordan, J., Eppler, J. M., Terhorst, D., Morrison, A., Linssen, C., Antonietti, A., Dai, K., Serenko, A., Cai, B., ... Plessier, H. E. (2020). *NEST 2.20.0* [Computer software]. Zenodo. <https://doi.org/10.5281/zenodo.3605514>
- Fernandes, A. M., Mearns, D. S., Donovan, J. C., Larsch, J., Helmbrecht, T. O., Kölsch, Y., Laurell, E., Kawakami, K., dal Maschio, M., & Baier, H. (2021). Neural circuitry for stimulus selection in the zebrafish visual system. *Neuron*, 109(5), 805-822.e6. <https://doi.org/10.1016/j.neuron.2020.12.002>

Flores-Herr, N., Protti, D. A., & Wässle, H. (2001). Synaptic currents generating the inhibitory

surround of ganglion cells in the mammalian retina. *The Journal of Neuroscience: The*

Official Journal of the Society for Neuroscience, 21(13), 4852–4863.

<https://doi.org/10.1523/JNEUROSCI.21-13-04852.2001>

Fürth, D., Vaissière, T., Tzortzi, O., Xuan, Y., Märtin, A., Lazaridis, I., Spigolon, G., Fisone, G.,

Tomer, R., Deisseroth, K., Carlén, M., Miller, C. A., Rumbaugh, G., & Meletis, K. (2018).

An interactive framework for whole-brain maps at cellular resolution. *Nature Neuroscience*,

21(1), 139–149. <https://doi.org/10.1038/s41593-017-0027-7>

Gale, S. D., & Murphy, G. J. (2014). Distinct Representation and Distribution of Visual Information

by Specific Cell Types in Mouse Superficial Superior Colliculus. *Journal of Neuroscience*,

34(40), 13458–13471. <https://doi.org/10.1523/JNEUROSCI.2768-14.2014>

Gehr, C., Sibille, J., & Kremkow, J. (2023). *Retinal input integration in excitatory and inhibitory*

neurons in the mouse superior colliculus in vivo (p. 2023.04.07.536092). bioRxiv.

<https://doi.org/10.1101/2023.04.07.536092>

Grossberg, S. (1983). The quantized geometry of visual space: The coherent computation of depth,

form, and lightness. *Behavioral and Brain Sciences*, 6(4), 625–657.

<https://doi.org/10.1017/S0140525X00017763>

Guo, L., & Kumar, A. (2023). Role of interneuron subtypes in controlling trial-by-trial output

variability in the neocortex. *Communications Biology*, 6(1), Article 1.

<https://doi.org/10.1038/s42003-023-05231-0>

Harris, K. D., & Mrsic-Flogel, T. D. (2013). Cortical connectivity and sensory coding. *Nature*,

503(7474), Article 7474. <https://doi.org/10.1038/nature12654>

Hong, Y. K., Kim, I.-J., & Sanes, J. R. (2011). Stereotyped axonal arbors of retinal ganglion cell

subsets in the mouse superior colliculus. *Journal of Comparative Neurology*, 519(9), 1691–

1711. <https://doi.org/10.1002/cne.22595>

- Hubel, D. H., & Wiesel, T. N. (1959). Receptive fields of single neurones in the cat's striate cortex. *The Journal of Physiology*, 148(3), 574–591.
- Jones, H. E., Grieve, K. L., Wang, W., & Sillito, A. M. (2001). Surround suppression in primate V1. *Journal of Neurophysiology*, 86(4), 2011–2028.
<https://doi.org/10.1152/jn.2001.86.4.2011>
- Kapadia, M. K., Ito, M., Gilbert, C. D., & Westheimer, G. (1995). Improvement in visual sensitivity by changes in local context: Parallel studies in human observers and in V1 of alert monkeys. *Neuron*, 15(4), 843–856. [https://doi.org/10.1016/0896-6273\(95\)90175-2](https://doi.org/10.1016/0896-6273(95)90175-2)
- Kardamakis, A. A., Pérez-Fernández, J., & Grillner, S. (2016). Spatiotemporal interplay between multisensory excitation and recruited inhibition in the lamprey optic tectum. *eLife*, 5, e16472. <https://doi.org/10.7554/eLife.16472>
- Kardamakis, A. A., Saitoh, K., & Grillner, S. (2015). Tectal microcircuit generating visual selection commands on gaze-controlling neurons. *Proceedings of the National Academy of Sciences*, 112(15), E1956–E1965. <https://doi.org/10.1073/pnas.1504866112>
- Kasai, M., & Isa, T. (2016). Imaging population dynamics of surround suppression in the superior colliculus. *The European Journal of Neuroscience*, 44(8), 2543–2556.
<https://doi.org/10.1111/ejn.13371>
- Kim, Y. J., Peterson, B. B., Crook, J. D., Joo, H. R., Wu, J., Puller, C., Robinson, F. R., Gamlin, P. D., Yau, K.-W., Viana, F., Troy, J. B., Smith, R. G., Packer, O. S., Detwiler, P. B., & Dacey, D. M. (2022). Origins of direction selectivity in the primate retina. *Nature Communications*, 13(1), Article 1. <https://doi.org/10.1038/s41467-022-30405-5>
- Knudsen, E. I., & Konishi, M. (1978). Center-Surround Organization of Auditory Receptive Fields in the Owl. *Science*, 202(4369), 778–780. <https://doi.org/10.1126/science.715444>
- Krieger, B., Qiao, M., Rousso, D. L., Sanes, J. R., & Meister, M. (2017). Four alpha ganglion cell types in mouse retina: Function, structure, and molecular signatures. *PLoS ONE*, 12(7), e0180091. <https://doi.org/10.1371/journal.pone.0180091>

- Lazaridis, I., Tzortzi, O., Weglage, M., Märtin, A., Xuan, Y., Parent, M., Johansson, Y., Fuzik, J., Fürth, D., Fenno, L. E., Ramakrishnan, C., Silberberg, G., Deisseroth, K., Carlén, M., & Meletis, K. (2019). A hypothalamus-habenula circuit controls aversion. *Molecular Psychiatry*, 24(9), Article 9. <https://doi.org/10.1038/s41380-019-0369-5>
- Liu, Y., Savier, E. L., DePiero, V. J., Chen, C., Schwalbe, D. C., Abraham-Fan, R.-J., Chen, H., Campbell, J. N., & Cang, J. (2023). Mapping visual functions onto molecular cell types in the mouse superior colliculus. *Neuron*, 111(12), 1876-1886.e5.
<https://doi.org/10.1016/j.neuron.2023.03.036>
- McIlwain, J. T., & Buser, P. (1968). Receptive fields of single cells in the cat's superior colliculus. *Experimental Brain Research*, 5(4), 314–325. <https://doi.org/10.1007/BF00235906>
- McLaughlin, T., & O'Leary, D. D. M. (2005). Molecular gradients and development of retinotopic maps. *Annual Review of Neuroscience*, 28, 327–355.
<https://doi.org/10.1146/annurev.neuro.28.061604.135714>
- McPeek, R. M., & Keller, E. L. (2004). Deficits in saccade target selection after inactivation of superior colliculus. *Nature Neuroscience*, 7(7), Article 7. <https://doi.org/10.1038/nn1269>
- Niell, C. M., & Scanziani, M. (2021). How Cortical Circuits Implement Cortical Computations: Mouse Visual Cortex as a Model. *Annual Review of Neuroscience*, 44(1), 517–546.
<https://doi.org/10.1146/annurev-neuro-102320-085825>
- Olsen, S. R., & Wilson, R. I. (2008). Lateral presynaptic inhibition mediates gain control in an olfactory circuit. *Nature*, 452(7190), Article 7190. <https://doi.org/10.1038/nature06864>
- Phongphanphanee, P., Marino, R. A., Kaneda, K., Yanagawa, Y., Munoz, D. P., & Isa, T. (2014). Distinct local circuit properties of the superficial and intermediate layers of the rodent superior colliculus. *European Journal of Neuroscience*, 40(2), 2329–2343.
<https://doi.org/10.1111/ejn.12579>

Reinhard, K., Li, C., Do, Q., Burke, E. G., Heynderickx, S., & Farrow, K. (2019). A projection

specific logic to sampling visual inputs in mouse superior colliculus. *eLife*, 8, e50697.

<https://doi.org/10.7554/eLife.50697>

Sachdev, R., Krause, M., & Mazer, J. (2012). Surround suppression and sparse coding in visual and barrel cortices. *Frontiers in Neural Circuits*, 6.

<https://www.frontiersin.org/articles/10.3389/fncir.2012.00043>

Sato, T. K., Haider, B., Häusser, M., & Carandini, M. (2016). An excitatory basis for divisive normalization in visual cortex. *Nature Neuroscience*, 19(4), Article 4.

<https://doi.org/10.1038/nn.4249>

Schiller, P. H., & Koerner, F. (1971). Discharge characteristics of single units in superior colliculus of the alert rhesus monkey. *Journal of Neurophysiology*, 34(5), 920–936.

<https://doi.org/10.1152/jn.1971.34.5.920>

Schiller, P. H., & Stryker, M. (1972). Single-unit recording and stimulation in superior colliculus of the alert rhesus monkey. *Journal of Neurophysiology*, 35(6), 915–924.

<https://doi.org/10.1152/jn.1972.35.6.915>

Solomon, S. G., Lee, B. B., & Sun, H. (2006). Suppressive Surrounds and Contrast Gain in Magnocellular-Pathway Retinal Ganglion Cells of Macaque. *Journal of Neuroscience*, 26(34), 8715–8726. <https://doi.org/10.1523/JNEUROSCI.0821-06.2006>

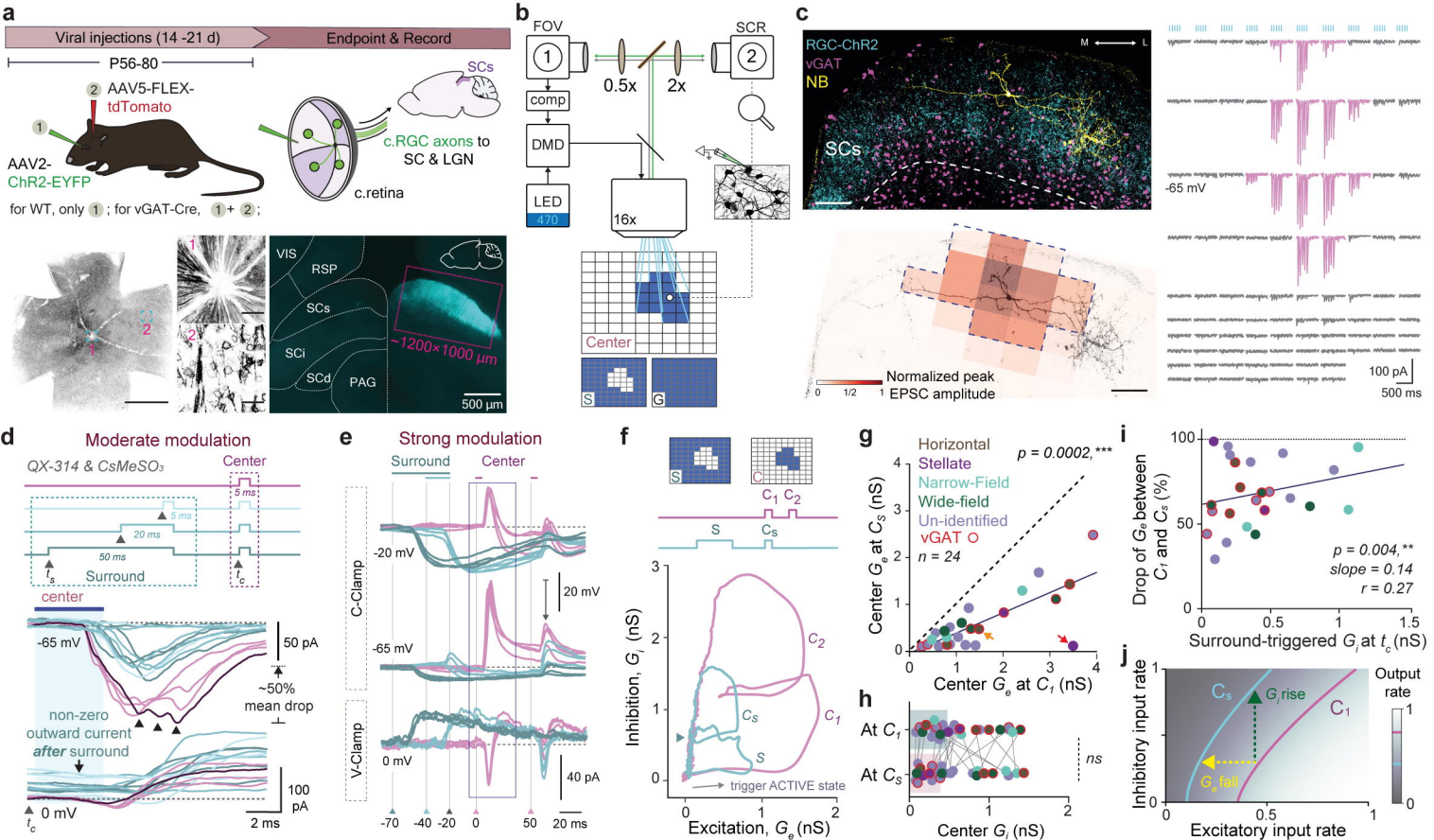
Wang, L., Herman, J. P., & Krauzlis, R. J. (2022). Neuronal modulation in the mouse superior colliculus during covert visual selective attention. *Scientific Reports*, 12(1), Article 1.

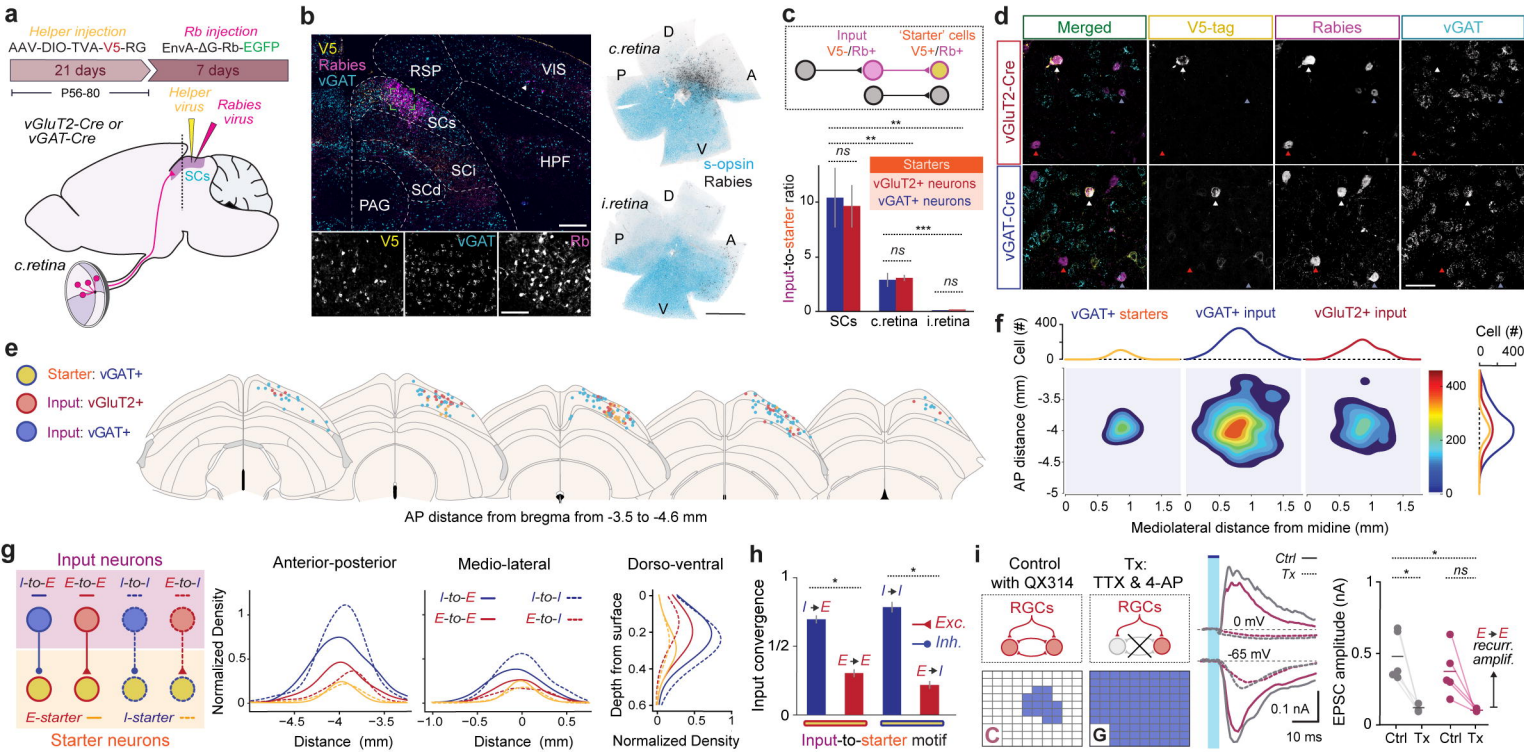
<https://doi.org/10.1038/s41598-022-06410-5>

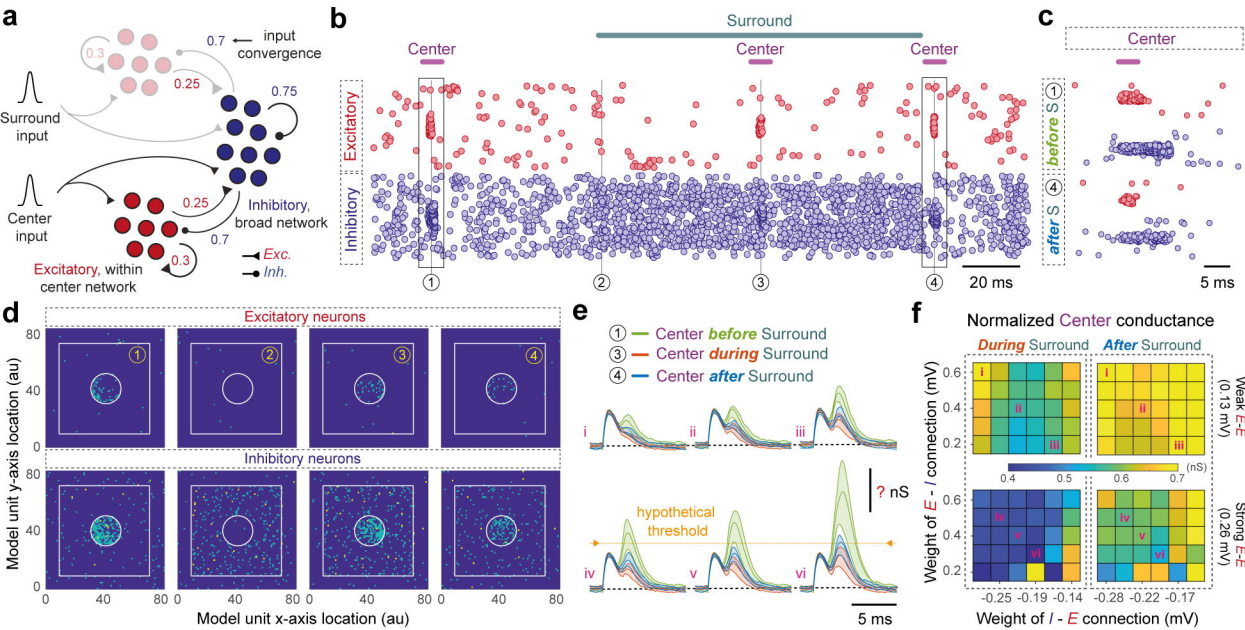
Wang, L., & Krauzlis, R. J. (2018). Visual Selective Attention in Mice. *Current Biology*, 28(5), 676-685.e4. <https://doi.org/10.1016/j.cub.2018.01.038>

Wehr, M., & Zador, A. M. (2003). Balanced inhibition underlies tuning and sharpens spike timing in auditory cortex. *Nature*, 426(6965), Article 6965. <https://doi.org/10.1038/nature02116>

- Wickersham, I. R., Lyon, D. C., Barnard, R. J. O., Mori, T., Finke, S., Conzelmann, K.-K., Young, J. A. T., & Callaway, E. M. (2007). Monosynaptic restriction of transsynaptic tracing from single, genetically targeted neurons. *Neuron*, 53(5), 639–647.
<https://doi.org/10.1016/j.neuron.2007.01.033>
- Zénon, A., & Krauzlis, R. J. (2012). Attention deficits without cortical neuronal deficits. *Nature*, 489(7416), 434–437. <https://doi.org/10.1038/nature11497>
- Zhang, X., Zhaoping, L., Zhou, T., & Fang, F. (2012). Neural Activities in V1 Create a Bottom-Up Saliency Map. *Neuron*, 73(1), 183–192. <https://doi.org/10.1016/j.neuron.2011.10.035>
- Zhang, Y., Kim, I.-J., Sanes, J. R., & Meister, M. (2012). The most numerous ganglion cell type of the mouse retina is a selective feature detector. *Proceedings of the National Academy of Sciences*, 109(36), E2391–E2398. <https://doi.org/10.1073/pnas.1211547109>









AAV2-ChR2-EYFP or AAV2-mCherry (Control)

